UiT
THE ARCTIC
UNIVERSITY
OF NORWAY

Department of Physics and Technology

Optical Trapping, Levitation and Tracking of Microparticles Using Waveguides

—

Øystein Ivar Helle

FYS-3941 Master's Thesis in Applied Physics and Mathematics

June 2014

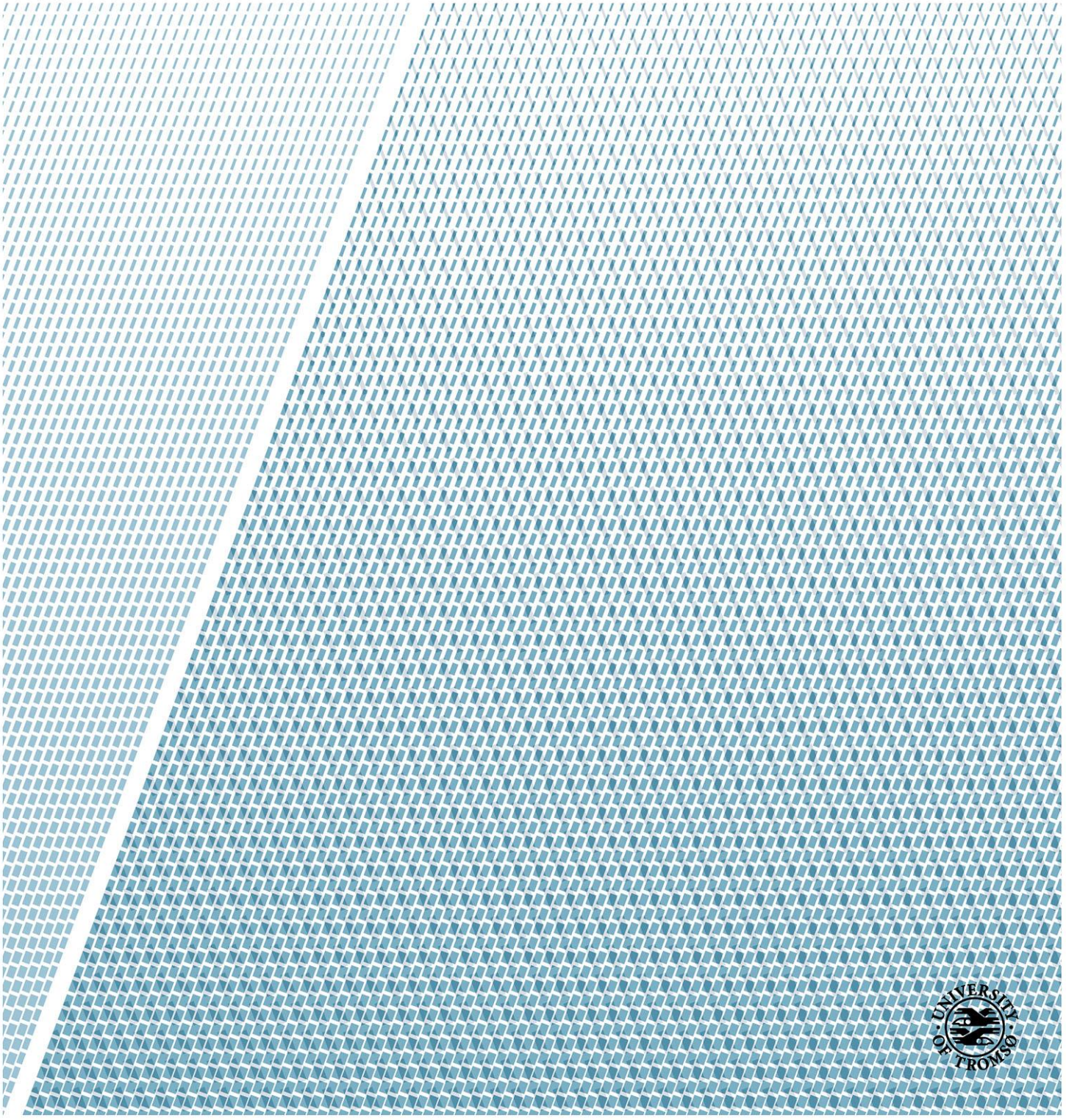

Abstract

Optical Trapping, Levitation and Tracking of Microparticles Using Waveguides

by Øystein Ivar Helle

Microparticles are trapped by optical forces created by the evanescent field present on the surface of an optical waveguide. An optical waveguide loop with an intentional gap is used to propel and stably hold the trapped particles. The particles are trapped in the gap of the loop by counter-diverging fields. Simulations indicate that particles trapped in the gap on a strip waveguide will be levitated. In this thesis a waveguide trapping setup is coupled with fluorescence imaging, and an algorithm is used to track the particles in 3 dimensions. The experimental results confirms optical levitation of microparticles trapped in the gap of a strip waveguide. Quantification of the noise associated with the setup and algorithm is performed to determine the precision of the method.

In a separate study, the trapping capabilities of strip and rib waveguides are compared. A rib waveguide loop differs from the strip waveguide loop, in that it has a guiding medium in the gap. This enables stable trapping along the gap, as a downward gradient force is present. Microparticles of different sizes are trapped using the rib waveguide, and a comparison with the strip waveguide is made.

Acknowledgements

I would like to thank my supervisor, Assoc. Prof. Balpreet Singh Ahluwalia. Thank you for leaving your office door open, and for sharing your knowledge. Your help has been priceless. I would also like to thank my co-supervisor Prof. O.G. Hellesø for inspiring talks. My appreciation goes out to the lab-rats in the basement; Jean-Claude, Adit, Susan and Firehun. Thank you all for your help. I thank my entire family for their support. Lastly, I thank my wife Tone. Thank you for being patient and for believing in me.

Contents

List of Figures

List of Tables

Chapter 1

Introduction

Waveguide trapping provides the ability to manipulate objects on waveguides using evanescent fields on top of the waveguide surface. The history of this field goes back to the papers published by Ashkin [1] in 1970, where experimental results on optical trapping of microparticles were reported for the first time. Ashkin used what is known as an optical tweezer, a single beam of light, to capture microparticles. An optical tweezer exploits the photons ability to transfer momentum to physical objects [2]. A Gaussian beam of light will impose either an attractive, or a repulsive force on objects in its path, thus pulling/pushing the object towards/away from the beam waist. The object will also become subject to a force pulling it in the direction of the propagating beam. These two forces are components of the force known as radiation pressure. A propagating mode of light in the core of a dielectric optical waveguide is the source of a leaking part of the field on top of the waveguide surface. This leaking field is known as the evanescent field and it has the same abilities; to transfer momentum to objects in its close vicinity by radiation pressure. The earliest experimental results showing radiation pressure in the evanescent field were performed by Kawata and Sugiura [3] which showed movement of microparticles on top of a prism confining a laser beam. The exponential decay of the evanescent field creates an intensity gradient attracting the particles on top of the waveguide, and radiation pressure propels the particles in the direction of beam propagation.

This thesis uses channel waveguides, and the first experimental results of manipulating objects on top of a channel waveguide were reported by Kawata and Tani in 1996 [4]. In their experiments a glass substrate with a channel waveguide was used, and particle velocities up to $14\mu m/s$ were reported. Optical propulsion has also been reported on Cs^+ ion exchanged waveguides on glass substrates [5], where particle velocity was linked

to particle size indicating higher velocity for larger particles. The biggest particles used in these experiments were $10\mu m$ polystyrene spheres giving speeds up to $33\mu m/s$.

In addition to propelling, the ability to stably trap particles is imperative with a lab-on-a-chip application in mind. To achieve stable trapping, a method of counter propagating beams [6] has been investigated. Here, particles are propelled along a glass Cs^+ ion-exchange waveguide. A counter propagating beam is inserted into the opposite end of the waveguide, resulting in that the particles change direction of propagation. The particles were shown to move in the direction of the beam which has higher power. If the beams were given equal power the particle would be trapped at a given location. The trapping was shown to last for several minutes, with the particle escaping the trap only by mechanical vibration, or by evaporation of the suspension fluid.

The research currently made in the physics department at the University of Tromsø has led to the development of a new waveguide design, specially suited for waveguide trapping of microparticles (figure 1.1). This design incorporates a waveguide loop with an intentional gap to enable stable trapping of microparticles ([7], [8]). The loop with a gap enables counter-propagating beams to meet, creating one or several stable trapping locations. The waveguides are made of Tantalum Pentoxide material which give high refractive index contrast, enhancing the intensity of the evanescent field. The experiments made on these structures showed promising trapping results. The research showed stable trapping of different sizes of polystyrene spheres($1\mu m - 5\mu m$). Red blood cells were also trapped.

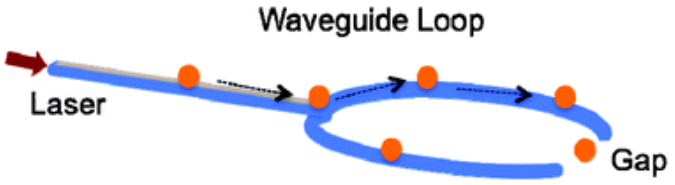

FIGURE 1.1: Waveguide loop with intentional gap[8].

Simulations have predicted that particles with a diameter of $1\mu m - 3\mu m$ will be levitated in the center of the gap on a strip waveguide loop with a gap separation of $10\mu m$.

1.1 Purpose

The purpose of this thesis is to experimentally verify the simulations predicting levitation of microspheres trapped in the gap of a strip waveguide loop. An algorithm that links the radius of the diffraction rings (of an out-of-focus particle), and the vertical position of the particle was developed in a previous thesis [9]. The algorithm was found unsuitable for use in bright/dark field applications due to the excessive noise from scattering in the

surrounding medium. In this thesis a fluorescence imaging module is integrated with the existing waveguide trapping setup. Fluorescence imaging offers reduced noise since all scattered light from the surrounding environment can be filtered out. The thesis will specify the algorithm for use with fluorescence imaging in attempt to measure the particles movement in 3 dimensions, both as they propel on straight waveguides and as they are trapped in the gap of a strip waveguide loop. Training on waveguide trapping was an important part of this thesis as all experiments were done independently.

The second part of this thesis is to compare the trapping capabilities of strip and rib waveguide geometries. While the strip waveguide is useful for tight trapping of particles in small gaps ($2\mu m$-$10\mu m$), the rib waveguide allow trapping and manipulation of particles on even larger gaps ($20\mu m$-$50\mu m$).

Chapter 2

Waveguide trapping and microscopy

This chapter will describe the properties of optical waveguides, and some theory about the evanescent fields used in waveguide trapping. Some basic microscopy principles will also be covered. Electromagnetic fields are described by Maxwells equations [2]. In this thesis we will assume non-magnetic materials and no free currents so Maxwells equations can be written on the form

$$\nabla \times \mathbf{E} = -\mu_0 \frac{\partial}{\partial t}\mathbf{H} \tag{2.1}$$

$$\nabla \times \mathbf{H} = \epsilon_0 n^2 \frac{\partial}{\partial t}\mathbf{E} \tag{2.2}$$

$$\nabla \cdot \mathbf{D} = 0 \tag{2.3}$$

$$\nabla \cdot \mathbf{B} = 0. \tag{2.4}$$

2.1 Total internal reflection and the evanescent field

When a ray of light hits a boundary between different materials, the refracted beam will depend on the difference in refractive index between the two materials, and the angle of

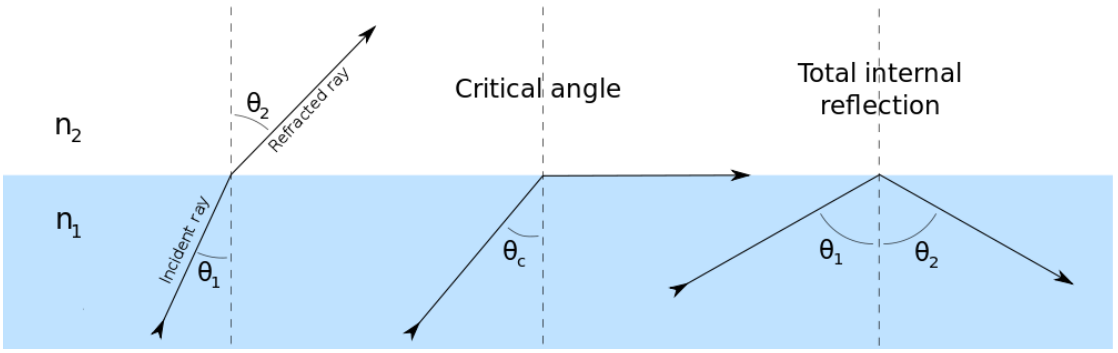

FIGURE 2.1: Reflection/Refraction at a boundary with $n_1 > n_2$ [10].

incidence . This relation is given by Snells law:

$$n_1 \sin\theta_1 = n_2 \sin\theta_2, \tag{2.5}$$

where it is observed that if $n_1 > n_2$, the refracted beam will be bent away from the surface normal (figure 2.1). If θ_1 increases, at some point the refracted beam will become parallel to the surface, ie.

$$\sin\theta_1 = \frac{n_2}{n_1}\sin 90^\circ \Rightarrow \theta_c = \arcsin\frac{n_2}{n_1}, \tag{2.6}$$

where θ_c is called the critical angle of incidence. When the incident angle θ_1 is greater than θ_c, no light will be refracted, and all the incident light is reflected. This is called total internal reflection (TIR).

Even though the field is totally reflected at the dielectric boundary shown in figure 2.1, there is a part of the field that is leaking through the boundary [11]. This leaking component is called the evanescent field, and it is present near the surface of dielectric optical waveguides supporting propagating modes of light.

To give a description of how the evanescent field behaves on the far side of a dielectric boundary, we can consider a transverse electric (TE) polarized wave that is totally reflected at a dielectric boundary as shown in figure 2.2. In this figure $\mathbf{K_i}$ and $\mathbf{K_r}$ denotes the incoming and reflected fields, respectively. In the case of a TE wave both the x-, and z-components of the electric field in medium 1 are zero, i.e $E_x^i = 0$ and $E_z^i = 0$. The incoming wave can thus be written as $E_{\text{TE}}^i = E_y^i \hat{y}$. Following the approach given by Fornel[12] the expressions for the field components at the boundary ($z = 0$) between the two materials are given by

$$E_y = \frac{2\cos\theta}{(1-n^2)^{1/2}} E_{\text{TE}}^i exp(-j(\delta_{\text{TE}})), \tag{2.7}$$

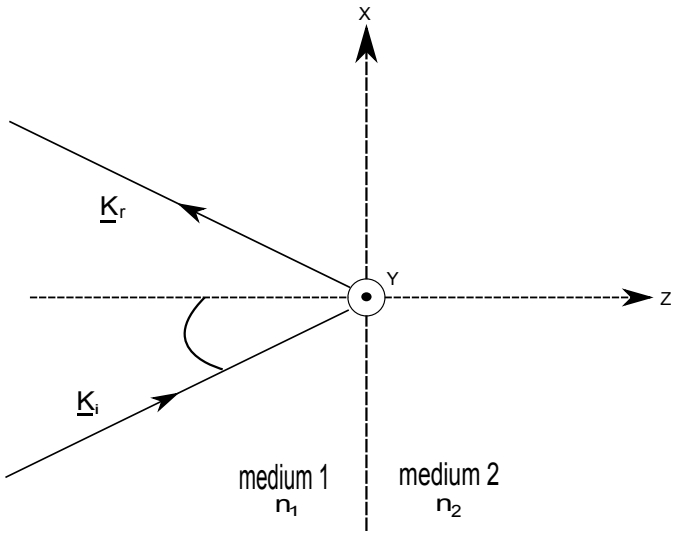

FIGURE 2.2: Beam of light interacting with a dielectric boundary with $n_1 > n_2$.

where $n = n_2/n_1$, θ is the incident beam angle with the dielectric boundary and $\tan\delta_{\text{TE}}$ is the solution to

$$\tan\delta_{\text{TE}} = \frac{(\sin^2\theta - n^2)^{1/2}}{\cos\theta}. \tag{2.8}$$

In the preceding equations we have ignored the x-dependence and time dependence for simplicity. As we move away from the boundary the field decays as

$$\mathbf{E}_{\text{TE}} = E^i_{\text{TE}} \frac{(2\cos\theta) exp(-z/d_p)}{\cos\theta + j(\sin^2\theta - n^2)^{1/2}} \hat{\mathbf{y}}. \tag{2.9}$$

From eq.(2.9) we notice the exponential decay of the evanescent field in medium 2. The penetration depth d_p is defined as the distance into medium 2 where the initial amplitude is reduced by $\frac{1}{e}$, and is given by

$$d_p = \frac{\lambda}{2\pi\sqrt{n_1^2\sin^2\theta - n^2}}. \tag{2.10}$$

The evanescent field can be thought of as an electrostatic field. If a dielectric of permittivity ϵ_2 and volume V is introduced in the field surrounded by a medium with permittivity ϵ_1, the potential energy of the field will change as shown by Stratton [13](p112-p114) :

$$U = \frac{1}{2}\int_{V_1} (\epsilon_1 - \epsilon_2)\mathbf{E}\cdot\mathbf{E_1} dv, \tag{2.11}$$

where $\mathbf{E}$ is the electrostatic field before the dielectric is introduced and $\mathbf{E_1}$ is the field afterwards. The medium is assumed to be linear and isotropic. Notice that when $\epsilon_2 > \epsilon_1$, the energy related to a small displacement is negative. The dielectric of permittivity ϵ_2 which is assumed free to move, will seek towards higher field intensities. This model describes the downwards/gradient force attracting particles towards a waveguide containing a propagating mode of light.

2.2 Optical waveguides

Optical waveguides are structures that can confine light. The geometry of such structures vary according to their usage, where the most common waveguide is the optical fiber used in tele-communications. Optical fibers are to prefer in communication since typical transmission wavelengths are in the near infrared band. The optical fiber thus offers high bandwidth. Typical wavelengths used are $\lambda = 850nm$, $\lambda = 1310nm$ and $\lambda = 1550nm$ [14], which are chosen to minimize losses. Other uses of optical fibers are in medical equipment [2], and in sensing[12]. This thesis will look at optical channel waveguides as a mean for trapping and transporting microparticles, with a lab-on-a-chip application in mind. Lab-on-a-chip refers to the ability to integrate one or several laboratory functions on a small chip[15]. In this thesis the lab-on-a-chip function would be to propel and trap microparticles, e.g enabling the operator to study single biological cells.

The most basic geometry of a waveguide is that of the slab waveguide (figure 2.3). This consist of 3 layers of dielectric material with different refractive indicies. If the refractive index of the middle layer (core) is higher than the surrounding materials, light can be confined within this layer due to total internal reflection. The cladding material could even be air as the refractive index of air lies around $n_{air} = 1$. In the next section we will see how light travels in an slab waveguide.

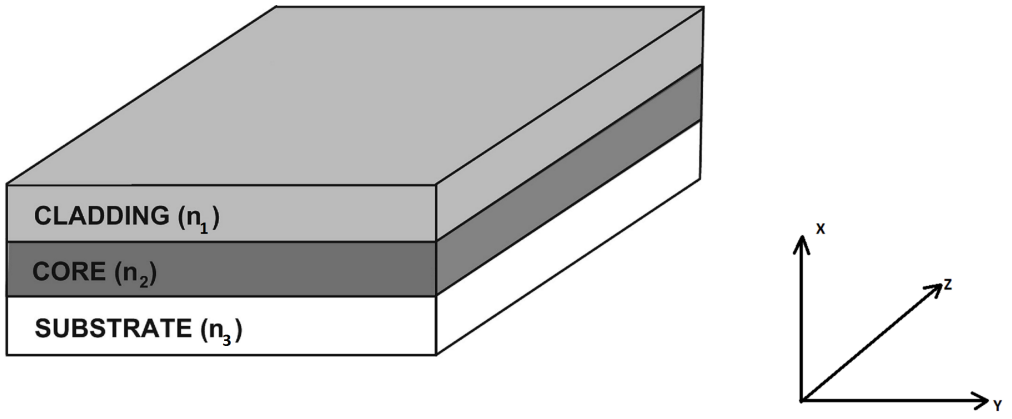

FIGURE 2.3: Geometry of a slab waveguide

2.2.1 The modes of a slab waveguide

Guided light in an optical waveguide travels in distinct modes. An optical mode can be thought of as a spatial distribution of the guided optical power. To give an understanding of optical modes one can consider the geometry of the slab waveguide in figure 2.3. If Maxwells equations and the proper boundary-conditions are used on the asymmetric (i.e $n_1 \neq n_3$) slab in figure 2.3, we will end up with the guiding condition showing the discrete nature of the propagating light. Without loss of generality we will consider only variations in the xz plane (figure 2.4), i.e $\partial/\partial y = 0$. Optical modes are named by how the components of the field are distributed. Transverse electric (TE) modes have the electric field component perpendicular to the plane of incidence (xz-plane), i.e in the y-direction. Transverse magnetic (TM) modes have the electric field components in the plane of incidence. This means that TE modes have the three components, E_y, H_x and H_z. TM modes have the three components E_x, E_z and H_y.

We will now look at how the guiding condition for TE modes in the asymmetric slab waveguide in figure 2.3 and 2.4 can be derived. The approach outlined in this section follows the one given by Lee[11].

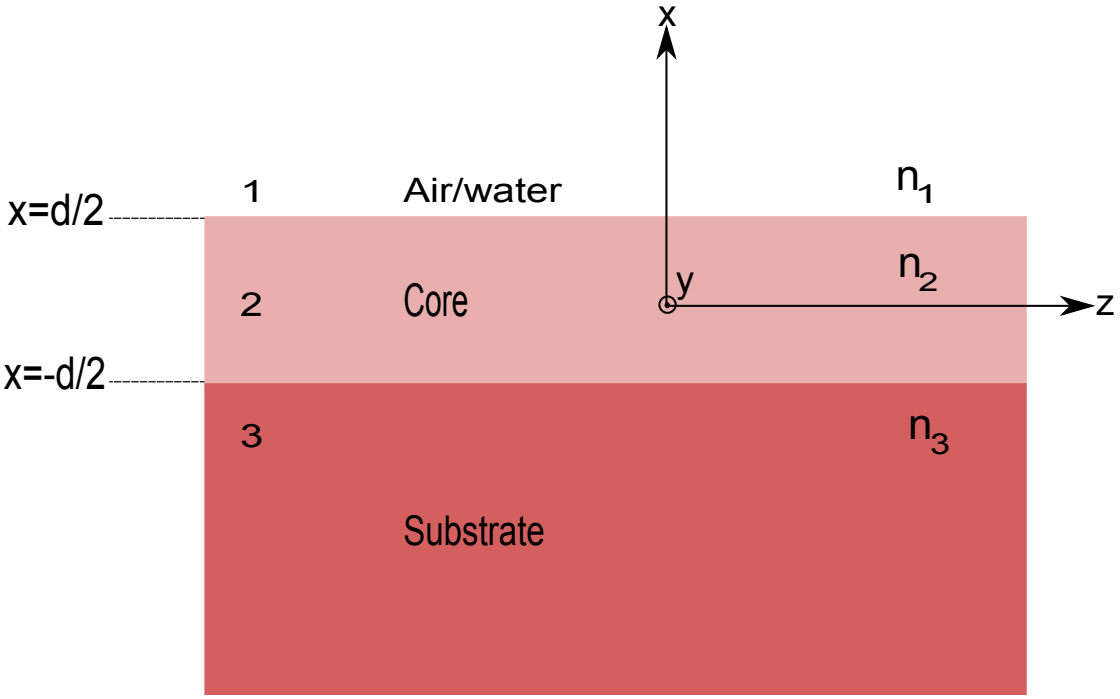

FIGURE 2.4: The asymmetric slab waveguide, xz-plane

If we assume that the field decays exponentially outside the guiding layer, and that it is a periodic function inside the core, we can write the electric field as

$$E_y = \left\{ \begin{array}{c} A_1 e^{-\alpha_{1x} x} \\ A_2 \cos(k_{2x} x + \psi) \\ A_3 e^{\alpha_{3x} x} \end{array} \right\} e^{-jk_z z} \quad \begin{array}{c} x > d/2 \\ x \leq d/2 \\ x < -d/2, \end{array} \tag{2.12}$$

where the transverse wave-numbers are related to the propagating wave numbers by

$$\alpha_{1x} = \sqrt{k_z^2 - \left(\omega \frac{n_1}{c_0}\right)^2}, \tag{2.13}$$

$$\alpha_{3x} = \sqrt{k_z^2 - \left(\omega \frac{n_3}{c_0}\right)^2}, \tag{2.14}$$

and

$$k_{2x} = \sqrt{\left(\omega \frac{n_2}{c_0}\right)^2 - k_z^2}. \tag{2.15}$$

We have assumed non-magnetic materials.

As was mentioned earlier, the parallel components of the field must be continuous at the boundaries between the different layers. Since we are investigating the TE modes this means that both E_y and H_z components must be continuous at $x = \pm d/2$ in figure 2.4. The magnetic field component H_z we find from eq.(2.1), by differentiating eq.(2.12).

$$H_z = \left\{ \begin{array}{c} \frac{-j\alpha_{1x}}{\omega\mu_0} A_1 e^{-\alpha_{1x} x} \\ \frac{-jk_{2x}}{\omega\mu_0} A_2 \sin(k_{2x} x + \psi) \\ \frac{j\alpha_{3x}}{\omega\mu_0} A_3 e^{\alpha_{3x} x} \end{array} \right\} e^{-jk_z z} \quad \begin{array}{c} x > d/2 \\ x \leq d/2 \\ x < -d/2 \end{array} \tag{2.16}$$

After applying the boundary conditions we end up with one transcendental equation at each boundary which must be solved either numerically or graphically. We call these equations the guiding conditions:

$$\tan(k_{2x} d/2 + \psi) = \frac{\alpha_{1x}}{k_{2x}} \tag{2.17}$$

and

$$\tan(k_{2x} d/2 - \psi) = \frac{\alpha_{3x}}{k_{2x}}. \tag{2.18}$$

To merge equations (2.17) and (2.18) into one equation, we first rewrite the two equations as

$$k_{2x} d/2 + \psi = \arctan(\frac{\alpha_{1x}}{k_{2x}}) \pm p\pi \tag{2.19}$$

and

$$k_{2x}d/2 - \psi = \arctan(\frac{\alpha_{3x}}{k_{2x}}) \pm p\pi, \tag{2.20}$$

where we have used the trigonometric identity

$$\tan x = \tan(x \pm n\pi).$$

If we for convenience let

$$\phi_1^{TE} = 2\arctan(\frac{\alpha_{1x}}{k_{2x}}) \pm p\pi \tag{2.21}$$

and

$$\phi_3^{TE} = 2\arctan(\frac{\alpha_{3x}}{k_{2x}}) \pm p\pi, \tag{2.22}$$

and then adding eq.(2.19) and eq.(2.20) we get

$$2k_{2x}d - \phi_1^{TE} - \phi_3^{TE} = 2p\pi \quad p = 0, 1... \tag{2.23}$$

which is the dispersion relation for TE modes. We observe from the dispersion relation that increasing k_{2x} (i.e increasing the frequency) or the thickness d, will increase the number of possible modes. This means that increasing the frequency of the propagating light, or using a thicker waveguide, will enable more modes to propagate in the waveguide.

2.2.2 Strip and rib waveguides

Several versions of the asymmetric slab waveguide are often used in practice. When the confining core is made into a narrow strip, the waveguide has strong confining possibilities as it is surrounded by lower refractive index material such as air or water, and the substrate beneath. This geometry is known as a strip waveguide (figure 2.5). The propagating modes in the waveguide must be evaluated in two dimensions to give an accurate description.

In case of a strip waveguide, the guiding layer is completely etched down to the substrate leaving a narrow strip of guiding material alone on top of the substrate (figure 2.5). If the guiding layer is only partially etched down, we get the rib waveguide geometry as seen in figure 2.6.

The strip waveguide confines light more tightly than the rib waveguide, and has less bending loss. The rib waveguide has less propagation loss due to sidewall roughness

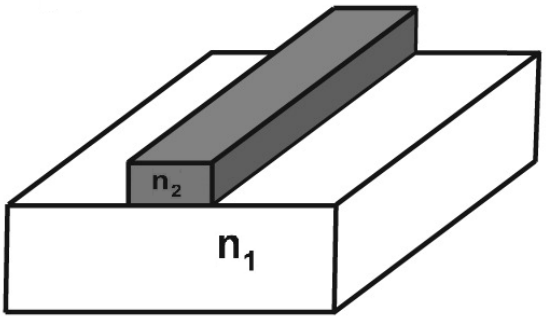

FIGURE 2.5: Geometry of a strip waveguide[16].

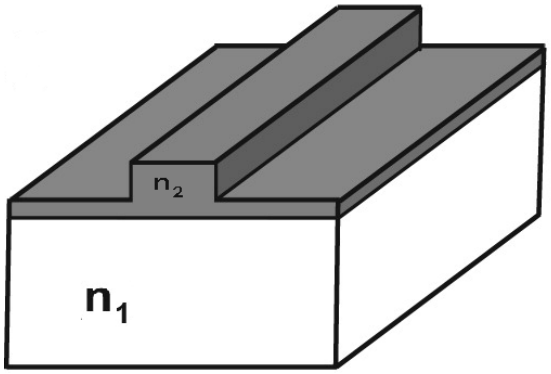

FIGURE 2.6: Geometry of a rib waveguide[16].

than the strip waveguide. Both rib and strip waveguides are used in the experiments done in this thesis. Section 3.1 discusses these geometries more thoroughly.

2.2.3 Waveguide losses

Loss in dielectric waveguides reduces the power, and consists of several factors; coupling, scattering, absorption and bending losses. Scattering loss is when a beam of light interacts with imperfections in the waveguide. There are two causes for scattering loss. Scattering caused by imperfections in the waveguide core, and scattering caused by imperfections on the waveguide surface. For the strip and rib waveguides described in this thesis, we mainly observe surface scattering from the side walls of the waveguides.

Absorption occur when the photon transmit its energy to an atom or an electron. The term propagation loss is used to describe the loss caused by absorption and scattering and is typically given in dB/cm.

In this thesis the waveguides used are made of Ta_2O_5. Propagation loss in this material has been experimentally tested [17] for straight waveguides as shown in table 2.1.

Input wavelength/power	Width(μm)	Propagation loss (dB/cm)
785nm/300mW	1	32.1
	1.5	6.5
	2	3.3
1070nm/680mW	1	29.6
	1.5	6.0
	2	2.7

TABLE 2.1: Propagation loss as function of waveguide width and wavelength for a $200nm$ thick Ta_2O_5 straight waveguide[17].

It is observed from table 2.1 that the propagation loss is less for wide waveguides than for narrow waveguides. Note that the results in table 2.1 are for a straight waveguides only, and in this thesis there will be a waveguide loop involved. Introducing the waveguide loop also introduces a new loss-factor; bend loss.

When a beam of light is propagating through a waveguide bend it will loose energy to the surroundings. This loss is referred to as bend loss. Following the approach given by Hunsperger [18], bend losses can be described by the velocity model. If we consider a waveguide bend, the phase velocity of a propagating mode will depend on the distance from the bend center. For a distance $R + X_r$ from the origin of the curve, the phase velocity of the propagating light will need to exceed the velocity of light in the surrounding material to keep up with the rest of the mode. The propagating mode will thus loose power as radiation in to the surrounding region. Consider figure 2.7 where the fundamental TE mode is assumed propagating along a waveguide bend. Let β_0 be the propagation constant of unguided light in medium 1, and β_z be the propagation constant for the propagating wave in the waveguide. From basic physics we know that the angular velocity $\frac{d\theta}{dt} = \omega$ must be the same for all points along the wavefront. This gives rise to two equalities:

$$R\frac{d\theta}{dt} = \frac{\omega}{\beta_z} \tag{2.24}$$

and

$$(R + X_r)\frac{d\theta}{dt} = \frac{\omega}{\beta_0}. \tag{2.25}$$

Combining these two equations give the distance X_r from the center-line of a waveguide bend of radius R, where the power starts to be radiated into medium 1 as observed in figure 2.7.

The amount of optical power lost through the bend is given by

$$\alpha = C_1 e^{-C_2 R}, \tag{2.26}$$

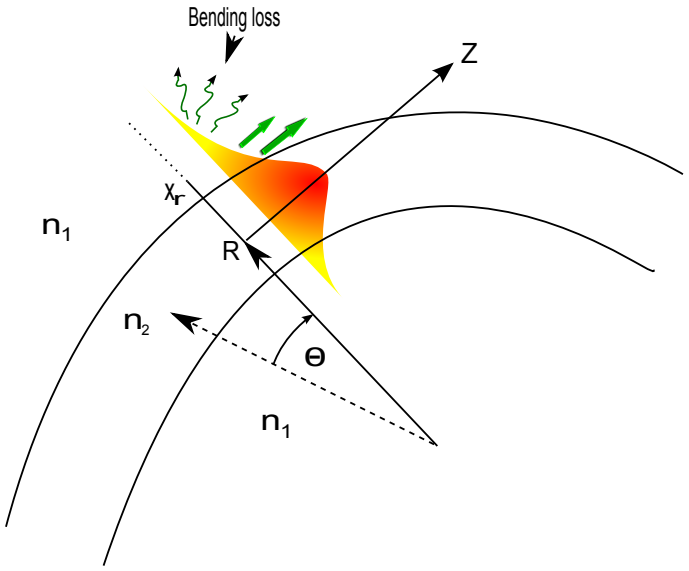

FIGURE 2.7: When the distance from the center of the curve exceeds a threshold X_r from the center-line of the waveguide, the power is radiated into the surrounding material.

where C_1 and C_2 are material constants and R is the loop radius. From eq.(2.26) it is observed that as the bend becomes more narrow, i.e R decreases, the bend loss increases exponentially. So more power is lost in sharp turns. In chapter 5 we will see this loss in practice when trying to propel particles on small loops on a rib waveguide.

2.3 Optical Trapping

Optical trapping of particles can be described in three regimes, according to the size of the particles involved. For particles with a diameter much smaller than the wavelength of the light used for trapping, Rayleigh scattering theory is used to describe the forces acting on the particles. If the particles diameter d is in the range of $\frac{\lambda}{20} < d < 30\lambda$, the forces acting on it can be described by Mie theory. For larger objects ($d > 30\lambda$) geometric optics can be used. In this thesis the particles are well into the Mie regime.

The forces acting on a particle in an evanescent field are the gradient force and the scattering force. The evanescent field is decaying exponentially from the waveguide surface, and the transverse decaying part of the field is the source of the gradient force. The gradient force acts on the particle in an attractive way, pulling it down towards the waveguide surface. The scattering force, has its source in the propagating part of

the field, thus causing the particle to propel in the direction of the propagating beam. To give a full description of the forces, Mie theory can be used. A less theoretic, but more intuitive and visual way to describe the forces acting on the particle is by the ray optics approach [19]. In figure 2.8 we see a dielectric particle suspended in water interacting with the evanescent field from the fundamental TE mode propagating in a slab waveguide as described earlier. The evanescent field for such a structure has a penetration depth d_p up to $200nm$ [20] and is exponentially decaying. From figure 2.8(a) we see that when a ray hits the water/sphere boundary the ray is both refracted and reflected. This results in a change of momentum at the sphere/water boundary, resulting in two forces $\mathbf{F_r}$ and $\mathbf{F_d}$. To see how the forces act on the sphere we first look at forces in the x direction. The forces due to reflection, $\mathbf{F_r}^i$ and $\mathbf{F_r}^o$, will cancel to first order [21]. If we look at a ray coming from A the sum of forces caused by refraction (i.e $\mathbf{F_d}$) will give a net force in the positive x direction, and a ray coming from B will give a force in the negative x direction. Since the field is exponentially decaying, the forces caused by a ray from B is stronger then the forces caused by a ray coming from A. This means that the sum of forces caused by refraction of rays coming from both A and B will result in a force attracting the sphere towards the waveguide surface, i.e in $-x$ direction. In the z direction the sum of the forces can be seen from the figure to give a positive force, thus propelling the particle along the waveguide. The sum of forces in both directions thus ends up in a forward pushing force $F_{Scatter}$, and an attractive force towards the beam waist F_{Grad} as seen in figure 2.8(b). If we consider the three dimensional case, a particle interacting with the evanescent field will be attracted towards the highest field intensity. For a single mode waveguide the highest intensity of the beam is at the center-line of the waveguide core. For a multimode fiber the highest beam intensity is typically found asymmetrical about the waveguide center-line. Later we will see polystyrene spheres submerged in water being trapped on a Ta_2O_5 waveguide surface.

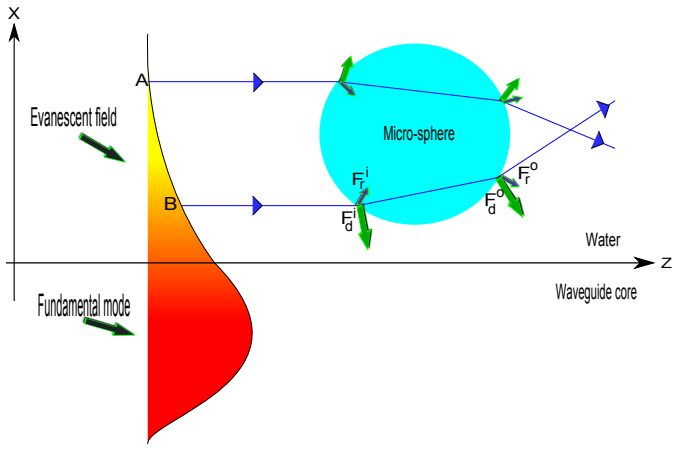

(a) Forces acting on the particle.

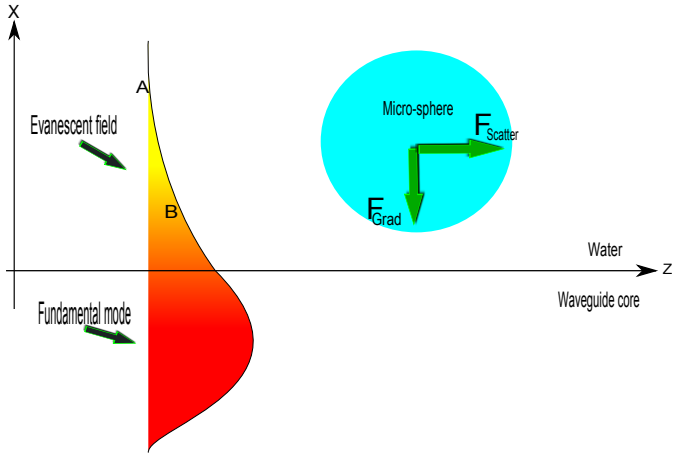

(b) Net force.

FIGURE 2.8: Ray approach for describing optical forces from the evanescent field on a microparticle. Sum of forces gives an attractive force F_{Grad} and a forward force $F_{Scatter}$ pulling the particle in the direction of beam propagation.

2.4 Microscopy techniques

Resolution in optical systems is defined as the smallest distance between to points in a sample which we can recognize as two different points [22]. To see small objects we use a microscope. The microscope consists of a series of lenses and mirrors used to create a two-dimensional magnified image. The resolution of the microscope will vary according to the choice of objective lens. The objective lens is the part of the microscope that collects the light which is to form the image. Figure 2.9 shows some objective lenses of different magnification. Numerical aperture NA describes the acceptance cone of the objective lens and is given by:

$$NA = n\sin(\theta), \tag{2.27}$$

FIGURE 2.9: Examples of objective lenses with magnification from 5X up to 60X [23].

where n is the refractive index of the material between the objective lens and the sample stage, often air (n=1). θ is the half angle of a cone of light entering the objective as seen in figure 2.10.

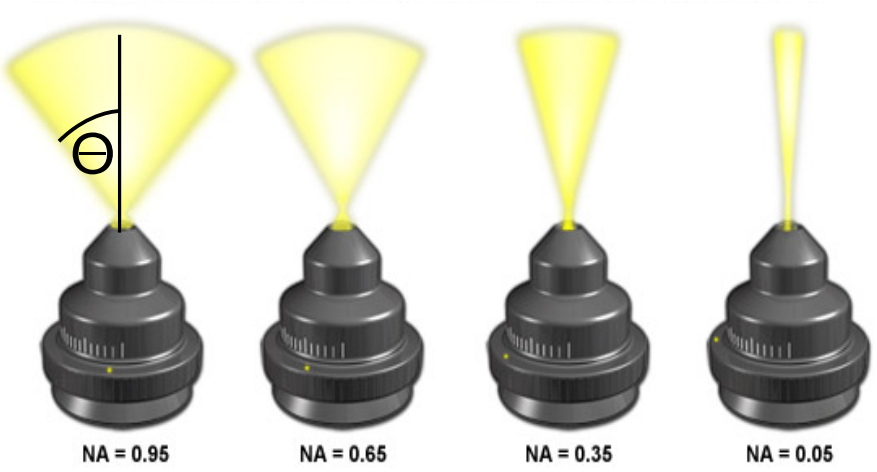

FIGURE 2.10: Cone size and shape versus numerical aperture [24].

From eq.(2.27) we see that for the typical medium between sample and objective, air, the maximum theoretical numerical aperture is $NA = 1$, i.e $n = 1$ and $\theta = 90°$. To compensate for this limitation, objectives which can be suspended in liquid are on the market. This will increase the numerical aperture up to 50% by the use of suspension oil ($n = 1.51$). Other suspension fluids used are water ($n = 1.33$) and glycerin ($n = 1.47$)

The optical microscope uses light to illuminate the sample, and often a CCD camera is used for acquiring images. The most basic technique used in microscopy is bright field microscopy. Here, all the light reflected from the sample and the surrounding surface is

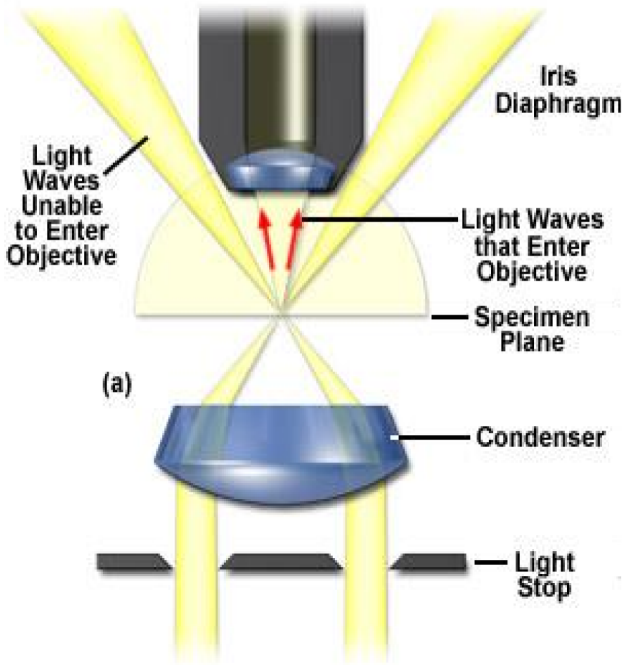

FIGURE 2.11: Example of a darkfield setup with illumination coming from under the sample [24].

collected by the lens to form the image. If less noise is required, dark field microscopy can be used.

In dark field microscopy the collected light comes from scattering in the sample. The mirror reflection is blocked using different techniques. One geometry which will give a dark field image of the sample is shown in figure 2.11. Here the light comes from under the sample, but the central part of the light is blocked before it is focused onto the sample. This results in that the microscope objective lens only captures the scattered light from the sample. Another approach to make a dark field microscope is to use the same lens as for bright field microscopy, and add a light-stopper as seen in figure 2.12. The light-stopper blocks the center of the ray, only letting peripheral light through thus producing a hollow cone of light. The light reflected back and displayed is then mostly light scattered from the sample, and not unscattered reflections from the sample/surrounding material.

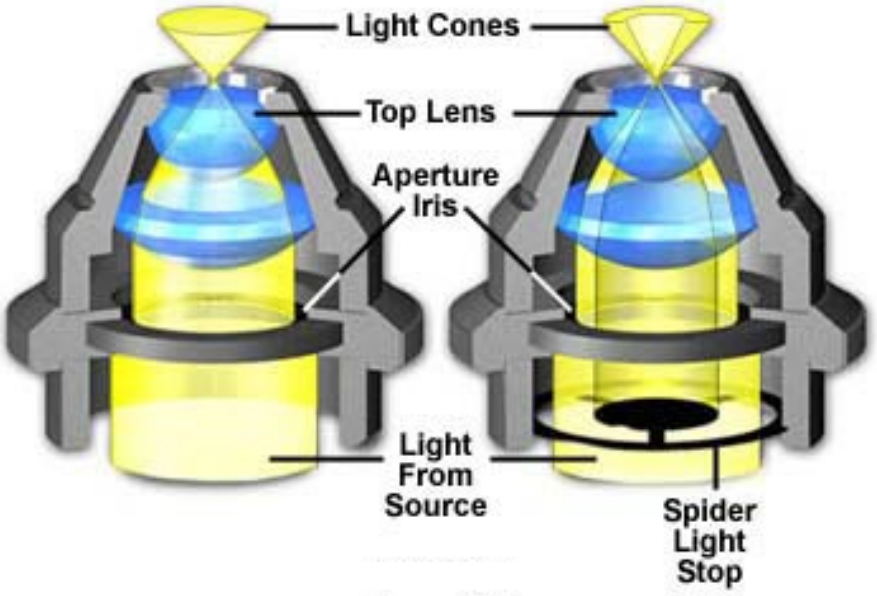

FIGURE 2.12: Abbe darkfield objective [25].

2.4.1 Fluorescence microscopy

If a photon of energy $E = \nu f$ is absorbed in an atom the atom will become excited from one energy state to another. The energy in the photon is absorbed by the electrons of the atom, causing the atom to increase in energy. The atom will make the transition back to the ground-state almost immediately $(0.1ns - 20ns)$[2], and in the process it looses energy. This lost energy may be in the form of another photon, depending on the energy level and type of atom involved. When the emitted photon lies in the visible range we call this process fluorescence, and the atom a fluorphore. The energy of the emitted photon is typically less than that of the absorbed photon since energy is lost in the process. This is known as Stokes shift which is illustrated in figure 2.13. If the energy of the emitted photon is less than the absorbed photon, the energy difference between them can be explained by thermal relaxation from one energy level to another, and the emittance of a photon between lower energy levels. This is illustrated in figure 2.14(b) and figure 2.14(c). If the emitted photon holds the same energy as the absorbed photon we have the case of figure 2.14(a). In this case the two curves of figure 2.13 will be on top of each other. Figure 2.14(d) shows a downward non-radiative transition followed by transition back to the higher energy level . In this process a photon of the same energy as the absorbed is emitted.

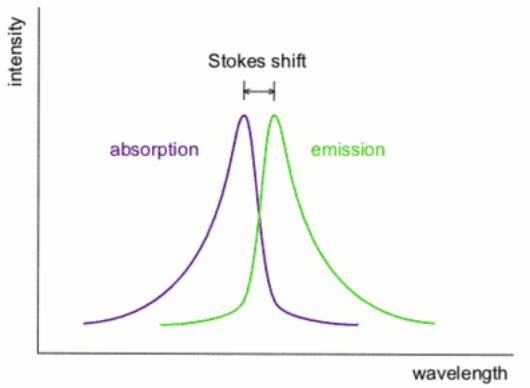

FIGURE 2.13: Stokesshift: Emitted photon has different wavelength than the absorbed photon [26].

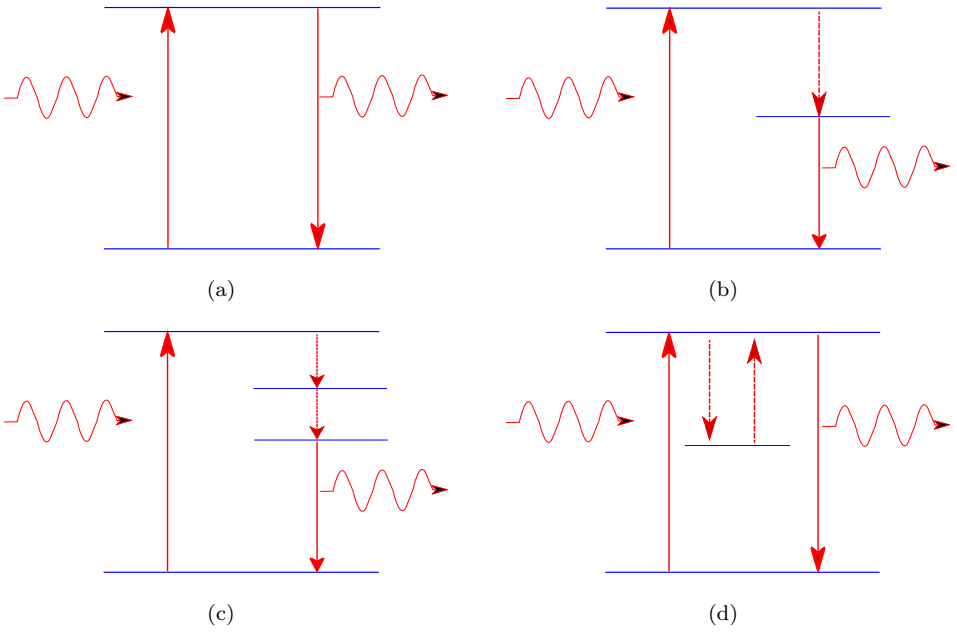

FIGURE 2.14: Different energy transitions caused by the absorption of a photon

Fluorescence microscopy is used as a mean for acquiring images without noise. In fluorescence microscopy the sample is stained with a fluorescent material, and a filter is used to block the mirror reflection from the light used to excite fluorescence, thus forming an image of the sample only. A setup that will produce fluorescence images is shown in figure 2.15.

The evanescent field can be use to excite fluorescence in particles on the waveguide surface. The trapping laser wavelength can be chosen to match the fluorescent wavelength of the particles used. Using the evanescent field to excite fluorescence instead of illuminating the particles from above, will result in fluorescence being excited in a part of the particle. The evanescent field is most dominant within $200nm$ from the waveguide

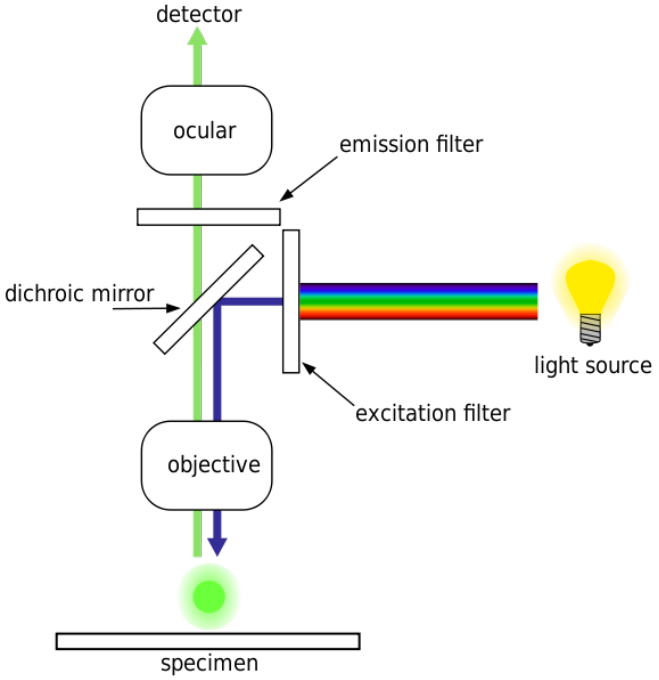

FIGURE 2.15: Example of setup for fluorescence microscopy [27].

surface, but can stretch up to $600nm - 700nm$. Only the part of the particle in contact with the evanescent field will start to illuminate. This can be used to study sections of a particle, e.g the cell wall of a red blood cell.

Methods for studying biological cells includes different fluorescence microscopy techniques. Total internal reflection fluorescent microscopy (TIRF) is one method that use the evanescent field to excite fluorescence in a sample. One form of TIRF is where the optical field comes from under the sample, through a prism, and is totally reflected at the boundary between the sample and the prism as illustrated in figure 2.16. Another form is objective based TIRF where the objective lens is used both for the excitation of fluorescence and for collecting the fluorescence light from the sample. High NA (> 1.45) objective lenses are needed for TIRF [28]. Other methods includes waveguide excitation fluorescence microscopy (WExFM) where the evanescent field of propagating light in a slab waveguide is used to excite fluorescence [29]. A new technique is presented by an Icelandic research group [30]. They use a waveguide where the refractive index of the cladding material is matched to the substrate resulting in a symmetric waveguide structure where the confining waveguide core cover the entire chip (SWExFM). The results from the Icelandic experiments were improved image quality, and better coupling of the excitation light compared to WExFM techniques.

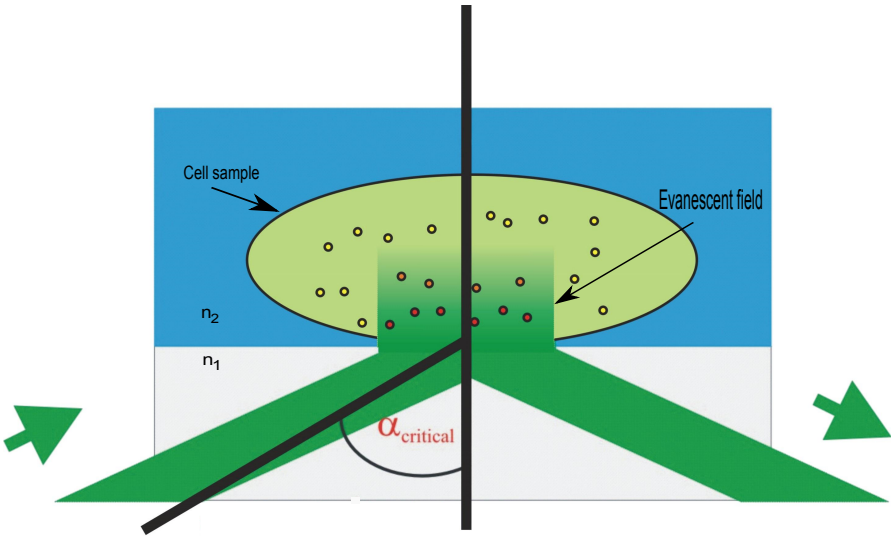

FIGURE 2.16: Excitation through a prism: The evanescent field stretches into the sample [31].

2.5 Diffraction through apertures

The wave nature of light causes diffraction when light interacts with a boundary. The intensity of the diffraction pattern created when imaging through a lens with circular aperture can be described by [2]:

$$I(x,y) = I_0 \left[\frac{2J_1(\pi D\rho/\lambda f)}{\pi D\rho/\lambda f} \right], \quad \rho = \sqrt{x^2+y^2}, \tag{2.28}$$

where f is the focal length, D is the diameter of the aperture, I_0 is the peak intensity and J_1 is the Bessel function of order 1. This pattern is known as an airy pattern and is always present when imaging (figure 2.17) through a circular aperture. The diffraction rings in the ideal situation of figure 2.17 and equation (2.28) have the highest intensity in the center. An microscope objective lens will not only be circular, it will also have spherical properties. Rays diffracted trough an objective lens will focus in different distances from the lens, according to the distance from the optical axis where they diffract. We call this spherical aberration, and it is illustrated in figure 2.18. From the figure it is seen that the marginal rays which diffract close to the edge of the lens, focus at a shorter distance from the lens than the paraxial rays, which diffract closer to the optical axis. This will impact the airy pattern in figure 2.17 such that the maximum intensity may not be in the middle of the pattern but might be in one of the diffraction rings, depending on where the focus is. In section 3.2 we use the diffraction rings created when imaging through an objective lens in an algorithm linking the distance from focus to the radius of the rings. In chapter 4 we use this algorithm to detect vertical movement of fluorescent microparticles.

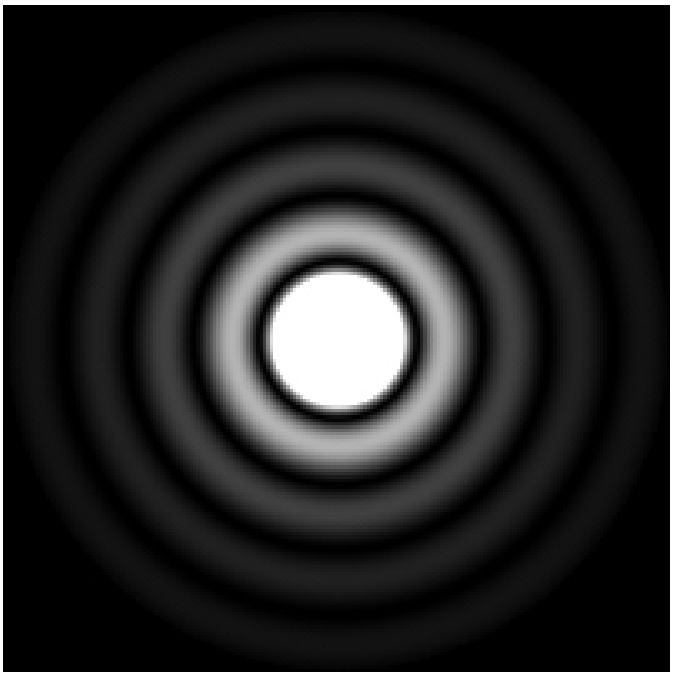

FIGURE 2.17: Airy pattern as a result of diffraction through a circular aperture [32].

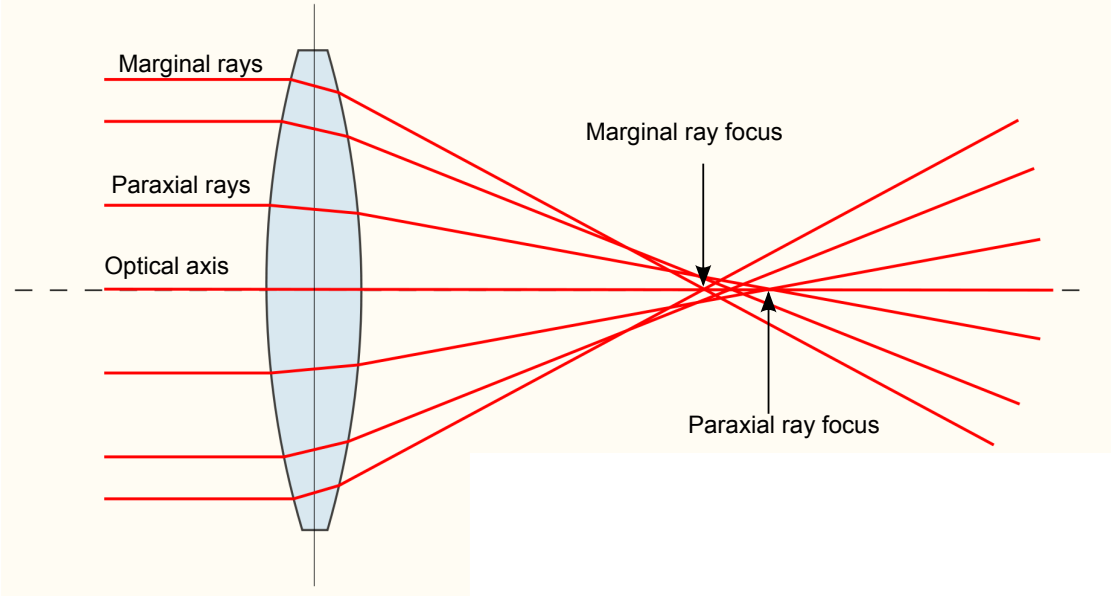

FIGURE 2.18: Spherical aberration: The marginal rays and the paraxial rays focus at different distances [33]

Chapter 3

Experimental methods and set-up

This chapter describes the methods, principles and equipment used when trapping particles, both on straight waveguides and using a waveguide loop. A method for tracking particles in 3 dimensions is described. The experimental setup both for fluorescence microscopy and bright field experiments is explained, and the equipment is listed. For the rest of this thesis the coordinate system is defined as in figure 3.1 with the x-direction being in the longitudinal direction of the waveguide, the y-direction being in the transverse direction of the waveguide, and the z-direction being the vertical direction. The schematic diagrams given in the following chapters are not to scale.

The reader is advised to apply the CD from the back-cover of the thesis to view some movies as we go along.

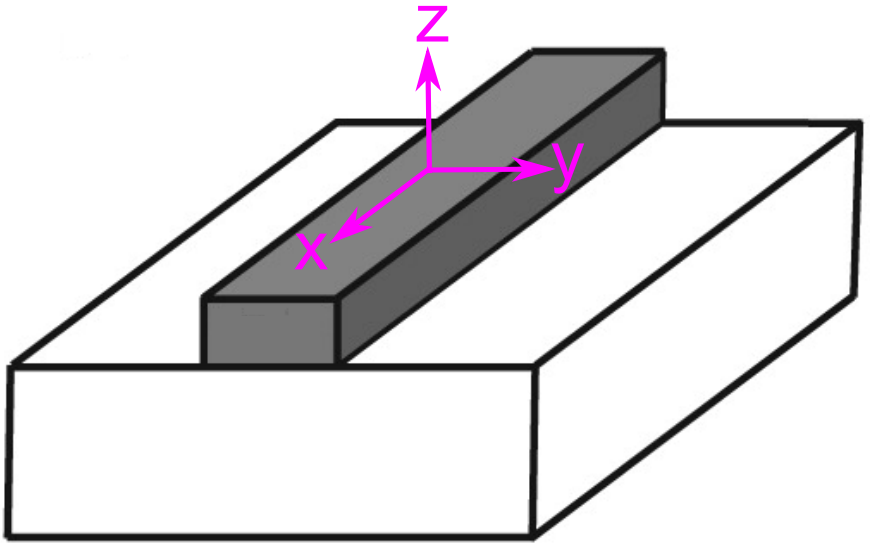

FIGURE 3.1: Axes used in the experimental part of the thesis. The x-direction is along the waveguide, the y-direction is transverse of the waveguide, and the z-direction is the vertical direction. Figure adapted from [16]

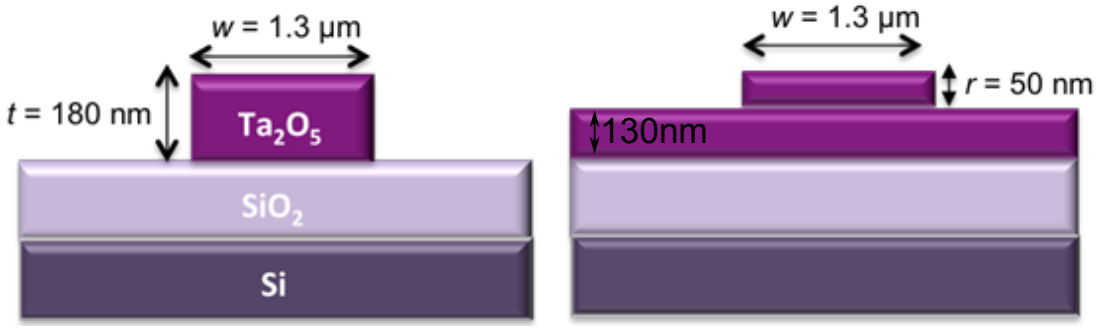

(a) Strip waveguide (b) Rib waveguide

FIGURE 3.2: Cross-section of the strip and rib waveguide geometries used in this thesis

3.1 Waveguide trapping

To enable optical trapping of microparticles using waveguides the evanescent field must be strong. To achieve this, a tight confinement of the guided field, and a high refractive index contrast between the waveguide and the surrounding layer is needed. The use of small cross sections of a high refractive index material such as Tantalum Pentoxide (Ta_2O_5) makes the evanescent field suitable for optical trapping. Both strip and rib waveguide geometries are used in this thesis. The strip waveguide (figure 3.2(a) and figure 2.5) offers a high gradient force, while the rib waveguide (figure 3.2(b) and figure 2.6) offers less absorption due to sidewall roughness. Unless otherwise stated, all the experiments in this thesis are on strip waveguides.

3.1.1 Straight waveguide

In waveguide trapping, particles are trapped by the evanescent field, which is most prominent within $150nm - 200nm$ distance from the waveguide. The evanescent field decays rapidly, but can stretch up to a distance of $600nm - 700nm$ for high refractive index material such as Ta_2O_5 or Si_3N_4 [34]. In order for a particle to be trapped it should remain within the evanescent field of the waveguide. A particle in close proximity of the waveguide will be attracted towards it, and held on top of the waveguide by the optical forces. The particle will also be propelled forwards by radiation pressure. **Movie 1** shows polystyrene particles of different sizes trapped on a straight $10\mu m$ wide waveguide. The particles are continuously propelled forwards. It can be seen that the particles are meandering, which is due to the intensity beating of the multiple modes supported by the waveguide. Particles meandering on a waveguide is illustrated in figure 3.3.

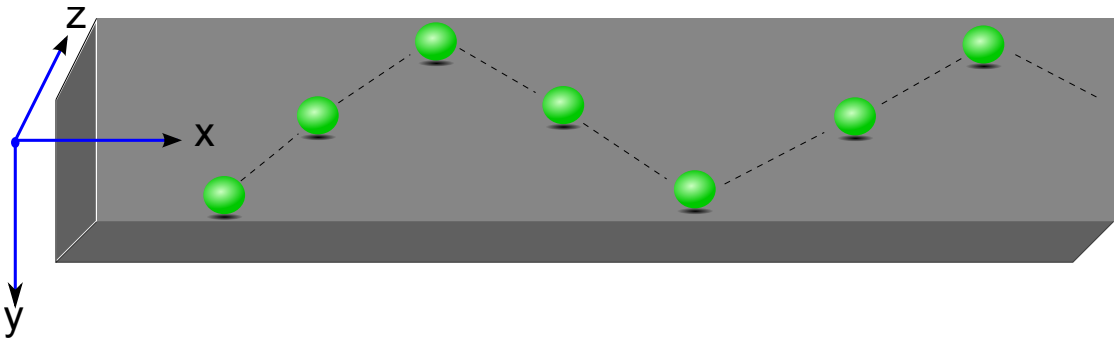

FIGURE 3.3: Particle propelling on straight waveguide. The meandering is due to intensity beating of multiple modes supported by the waveguide.

3.1.2 Waveguide loop

Particles trapped on straight waveguides are continuously propelled forwards, as we saw in **Movie 1**. To enable stable trapping of particles at a given location a new waveguide design is used. The design incorporates a waveguide loop with an intentional gap. In the gap, the counter diverging fields from the same source meet creating one or several stable trapping locations. Figure 3.4(a) show a top view a a waveguide loop. This particular loop has a radius of $100\mu m$ and a gap separation of $10\mu m$. Figure 3.4(b) show a 50X dark field image of the gap where we can see the escaping light from the waveguide ends interfering. **Movie 2** show a top view of a waveguide loop with particles on top of it. The particles are suspended in water. Laser is coupled on to the straight part of the waveguide, and at the y-branch the optical power divide in to the two arms. Particles in the vicinity of the waveguide are trapped and propelled along the waveguide, and delivered to the gap by the waveguide loop arms. **Movie 3** show a particle trapped in the gap of a waveguide loop. The counter diverging fields escaping the two waveguide ends create stable trapping for the particle. The particle holds its position as long as the laser is on.

The forces acting on particles in the gap of the waveguide loop will depend on the gap separation distance, in addition to the type of waveguide used. The strip waveguide has no guiding medium in the gap (as seen in figure 3.5(a)), thus there is no downward pulling gradient force acting from the gap on the particles in the gap . The only light that transfers momentum to the particles in the gap of a strip waveguide is the light diverging out from the waveguide ends. The trapping force of the strip waveguide thus rapidly decrease as the gap separation distance increase.

The gap of the rib waveguide loop offers a guiding layer between the waveguide ends as seen in figure 3.5(b). The guiding layer in the gap, which will contain a propagating mode of light, will be the source of an evanescent field. Thus, for a rib waveguide loop,

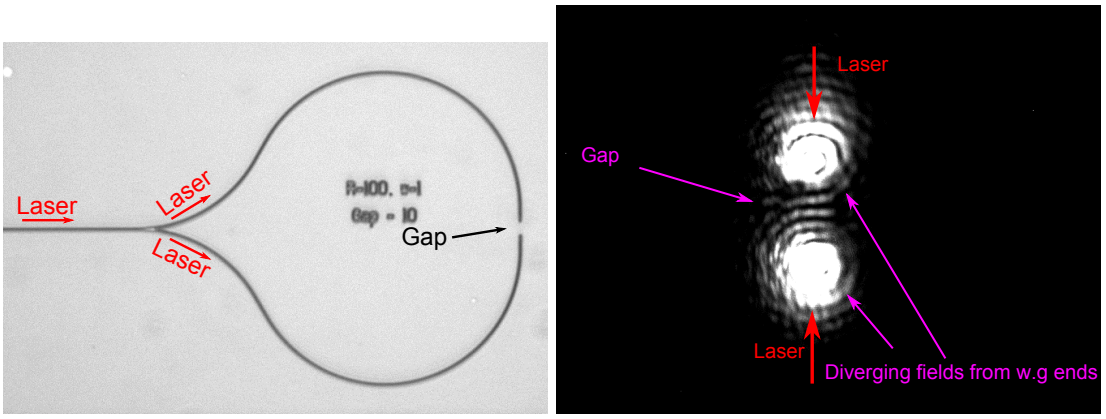

(a) Waveguide loop top view (b) 50X Dark field image of the fields in the gap

FIGURE 3.4: (a) Top view of a waveguide loop. The Laser is coupled on the straight part and separates in the y-branch. (b) At the gap the counter diverging fields from the same source meet.

there is a downward pulling gradient force acting from the guiding medium in the gap on particles trapped in the gap. This means that it should be easier to trap particles in larger gaps on rib waveguides, than on strip waveguides.

Simulations of the optical forces acting on particles in the gap, and the intensity of the electric fields in the gap of the waveguide loop have been made by O.G. Hellesø. Figure 3.5(c) show the simulated normalized electric fields in the gap of a strip waveguide. Figure 3.5(d) show the simulation of the normalized electric field in the gap of a rib waveguide. It can be seen from the figures that the rib waveguide offers several maxima in the guiding layer in the gap. The gap of the strip waveguide loop is seen to offer maxima above the waveguide chip.

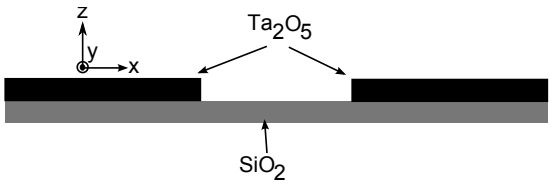

(a) Gap of a strip waveguide loop

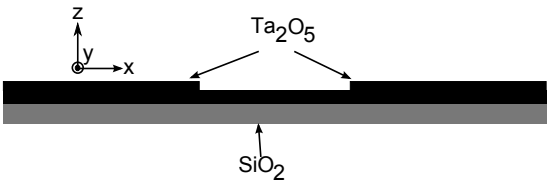

(b) Gap of a Rib waveguide loop

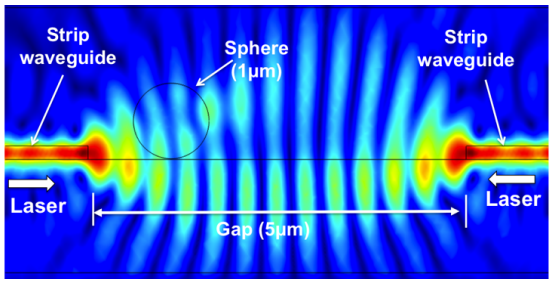

(c) Simulated electric field in the gap of a strip waveguide

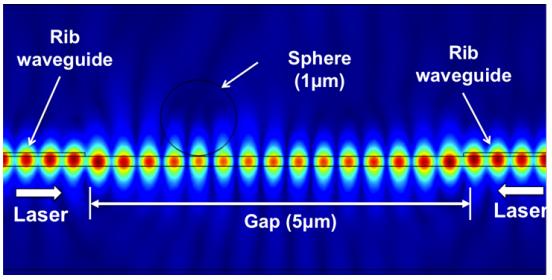

(d) Simulated electric field in the gap of a rib waveguide

FIGURE 3.5: Strip and rib waveguide loops differ in that there is no guiding material in the gap of the strip waveguide, while for the rib waveguide there is. The simulations in (c) and (d) show the normalized electric field distribution for the two geometries for a gap size of $5\mu m$.

The notion of figure 3.5(c), that the field gradient is stronger above the waveguide chip in the gap of a strip waveguide has been simulated for different gap sizes. The simulations indicate that the vertical force acting on particles in the gap of a strip waveguide starts out negative near the waveguide ends, but for some distance along the gap the force turns positive, thus the particles should be levitated. This is true for sufficiently large gap separations on strip waveguides. The simulated vertical (z-direction) force f_z acting on a particle with a diameter of $2\mu m$ in a $10\mu m$ wide gap on a strip waveguide is shown figure 3.6(a). The force turns positive at some distance along the gap, indicating levitation of the particle. If we zoom in on the distance along the gap where the vertical force turn positive we get figure 3.6(b), where we can see that the force becomes positive at around $3.4\mu m$ distance from the waveguide end. The horizontal (x-direction) force f_x along the gap is shown in figure 3.6(c). At some distance from the waveguide end f_x oscillates around 0. A stable trapping location x_s is identified as the point where a restoring force is present, i.e $f_x(x_s - \xi) > 0$ and $f_x(x_s + \xi) < 0$ for some small interval ξ in the neighborhood of x_s. If the particle move away from a stable location, the restoring force will bring the particle back. For an unstable trapping location, i.e $f_x(x_s - \xi) < 0$ and $f_x(x_s + \xi) > 0$, a small displacement away from the trapping location will result in that the particle is knocked out. Both stable and unstable trapping locations are shown in figure 3.6(c).

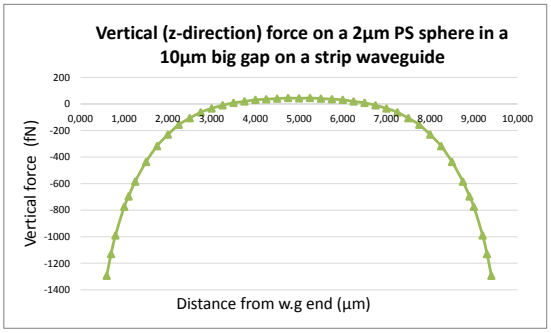

(a) Vertical force as function of distance from waveguide end.

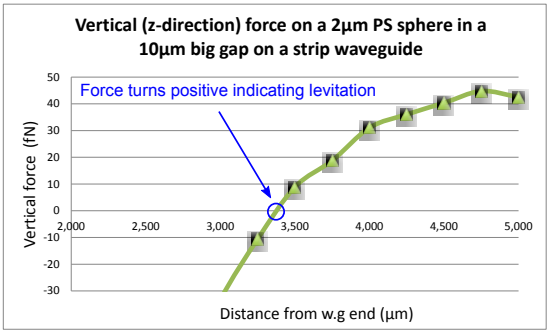

(b) Vertical force as function of distance from waveguide end zoomed in on the zero-crossing

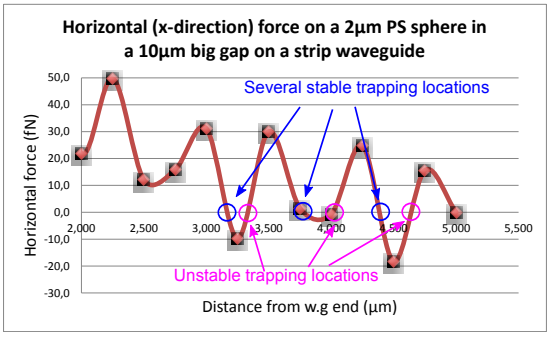

(c) Horizontal force as function of distance from waveguide end

FIGURE 3.6: Simulations of the force on a $2\mu m$ big particle in a $10\mu m$ big gap. The vertical force turn positive at around $3.4\mu m$ from the waveguide end, indicating levitation. Notice that the horizontal force oscillate around 0 creating several stable trapping locations.

The result from simulations indicate that particles of different sizes will be levitated in the gap of strip waveguides with a gap separation of $10\mu m$. The distance z above the waveguide chip the particles are trapped has also been simulated. Figure 3.7(a) show the vertical force as a function of distance above the waveguide chip for a $2\mu m$ big particle in a $10\mu m$ wide gap on a strip waveguide. The figure show the stable trapping location as the particle is levitated upwards. The simulation shows two stable locations at around $1.2\mu m$ and $3.2\mu m$ above the waveguide chip. These are illustrated in figure 3.7(b)

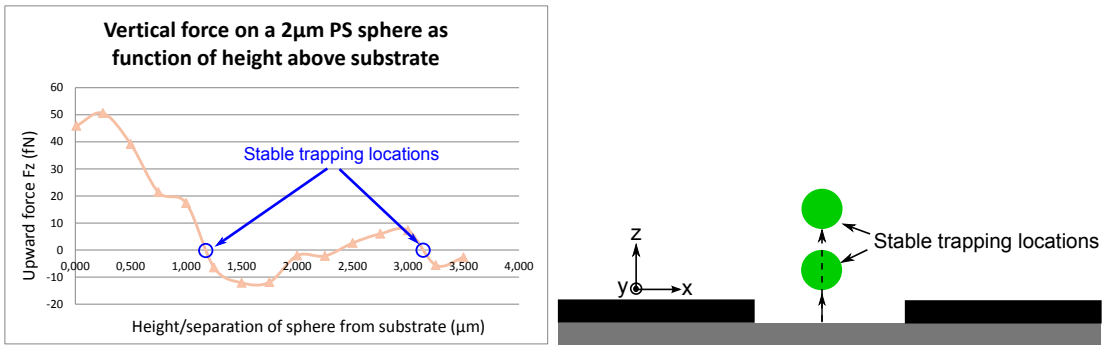

(a) The simulated vertical force as function of distance (b) Simulated vertical force show two stable positions above waveguide chip for a particle with diameter of above the w.g
$2\mu m$

FIGURE 3.7: Simulation of the vertical force as a function of the height above the waveguide chip for a $2\mu m$ big particle in a $10\mu m$ wide gap. (a) The simulation predicts two stable distances above the substrate where the particle is trapped, which are illustrated in (b).

3.2 Particle tracking in 3D using fluorescent images

To confirm the simulated levitation of particles in the gap of the strip waveguide loop, an algorithm is used track the vertical position of a particle. For detecting this vertical displacement of microparticles we can utilize the notion of equation 2.28 where we saw that there is always a diffraction pattern present when imaging through an spherical aperture. A method developed recently take advantage of the the diffraction rings created when the particle is imaged away from focus ([9],[35]). As we move away from focus the diffraction pattern keeps its symmetry, but the radius of the outermost ring change, thus there is a link between the distance from focus and the radius of the outermost diffraction rings. This is illustrated in figure 3.8 where we see a linear relationship between the vertical distance z from focus, and the radius r_0 of the outermost diffraction ring.

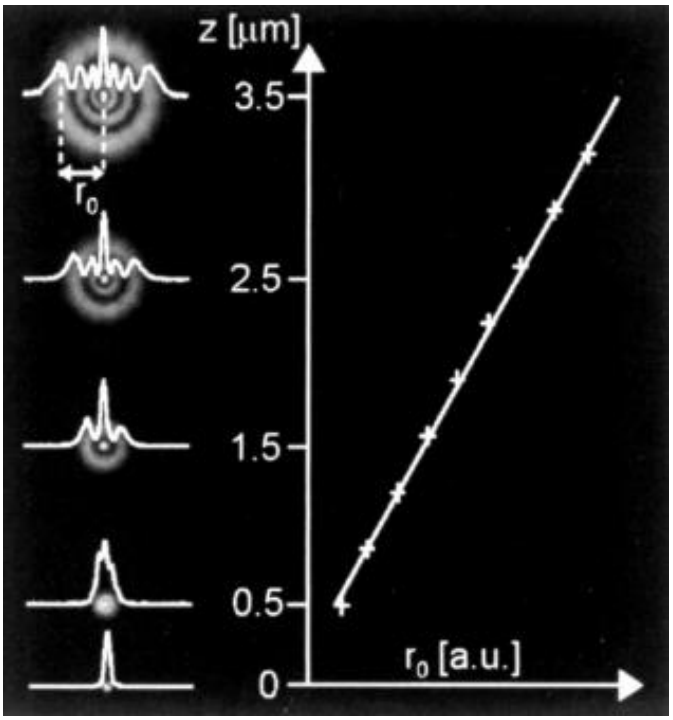

FIGURE 3.8: Linear relationship between the radius r_0 of the outermost diffraction ring created when imaging through a spherical aperture, and the vertical distance z from focus [35].

The algorithm used in this thesis takes as input images of fluorescent particles (as seen in figure 3.9(a)) with their diffraction rings visible. The algorithm can be summarized in these few steps:

- Detect the center of the intensity distribution
- Find the average intensity of concentric circles around the center of the original image to get a 1-dimensional intensity distribution. Figure 3.9(b) show the 1-dimensional intensity distribution of the image in figure 3.9(a)
- Use a 1st order derivative peak detecting algorithm to estimate the location of the outermost peak in the 1-dimensional intensity distribution. This is the first estimate for the radius of the outermost diffraction ring.
- Fit a 4th order polynomial around the first estimate to further improve the precision. A polynomial is used to allow for more variation in the peak. The final estimate for the radius of the outermost diffraction ring is then the maximum point of the 4th order polynomial.
- Use the calibration of the system to map the change in radius (in pixels) to change in vertical displacement (in μm).

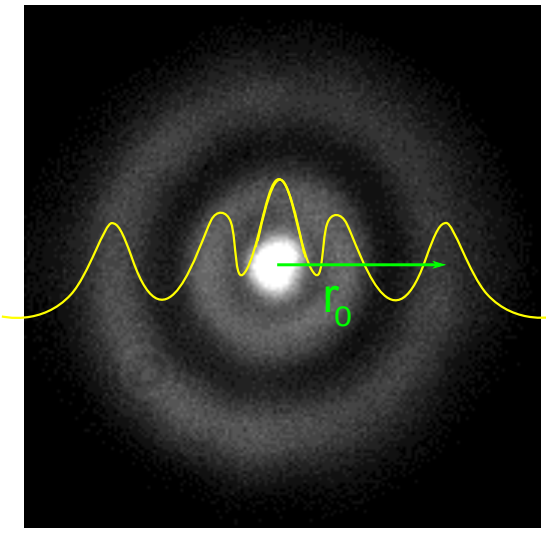

(a) Off focus image of fluorescent particle. We need to find an estimate for the radius of the outermost diffraction ring r_0.

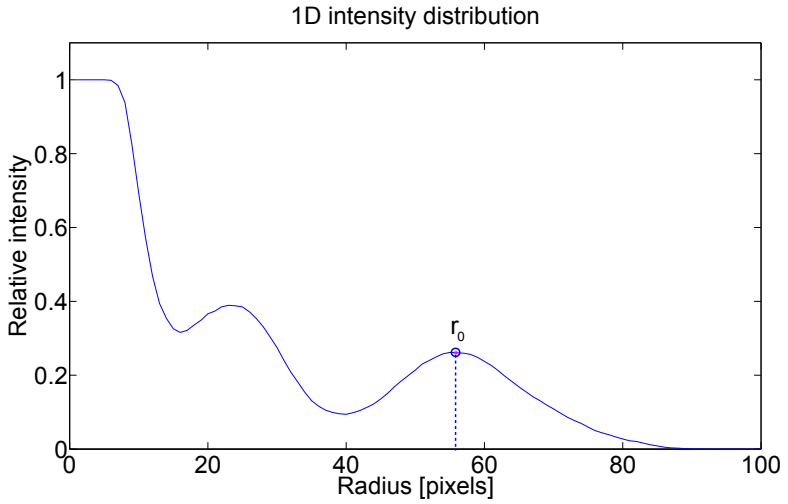

(b) 1D representation of the intensity distribution where we see the estimate r_0 of the outermost diffraction ring

FIGURE 3.9: The algorithm for detecting vertical displacement of microparticles use images of the diffraction rings. The intensity distribution is represented in 1-dimension. The radius of the outermost diffraction ring r_0 is the distance to the outermost peak in the 1-dimensional intensity distribution

To get the mapping from radius of the diffraction rings to vertical displacement a calibration is done. Fluorescent particles are left to stick on the waveguide surface. The particles can then be imaged in a series of images, where for each image the focus is changed by a constant amount. Tracking the change in diffraction ring radius of the immobilized particles, and comparing it with the distance from focus give the desired mapping.

A method to find the actual size of one pixel in the horizontal plane is to image immobilized particles through several images, where for each image the camera/microscope (which is mounted on a translation stage) is moved by a constant and known amount. The size of one pixel will then be the the distance the camera has moved divided by the length (in pixels) of the line between the particle. Figure 3.10 show an example of this.

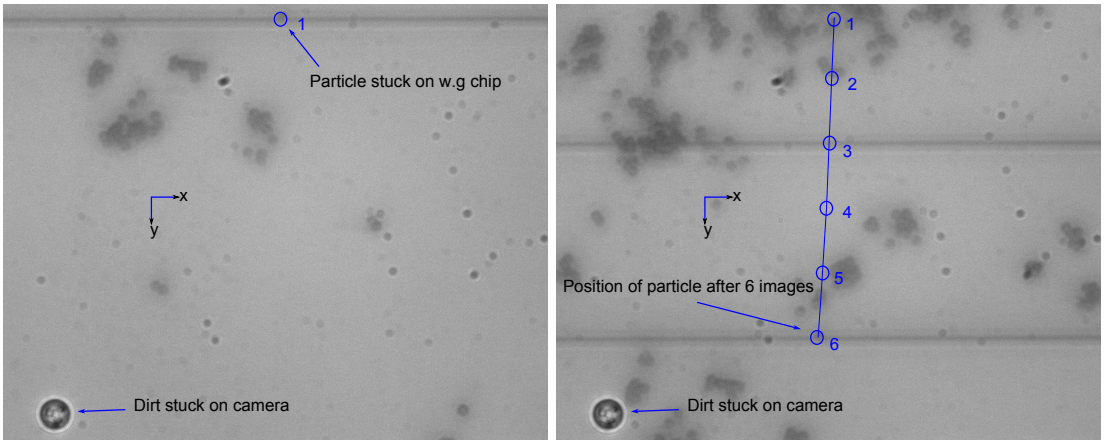

(a) A particle stuck on the waveguide is marked by the blue ring

(b) The same stuck particle is followed trough several images, where for each image the camera is moved by a constant amount. Here we see the 6th image in a series.

FIGURE 3.10: Calibration in the horizontal plane. A particle stuck on the waveguide chip is followed through several images. Before each image is acquired the camera is moved by $10\mu m$.

The entire process for tracking particles in 3 dimensions is summarized as:

- Before experiments starts: Calibrate the system in the vertical direction by making calibration curves for the different particle diameters that will be used in the experiments. This is done to get the mapping from radius of the outermost diffraction ring to change in vertical displacement.
- Acquire a movie of the fluorescent particle under investigation. The movie should be out of focus so that the diffraction ring is visible. The concentration of particles must be low to reduce noise contributed by interfering particles.
- Use the algorithm described above to translate the change in diffraction ring radius to change in vertical displacement.
- To track the particle in the horizontal plane, use the calibration from figure 3.10 to find the actual size of one pixel. Track the particles center through the movie to get its relative displacement, measured in pixels. Use the calibration to map from pixels to units of length. The center of the particle is found as the center of the intensity distribution (figure 3.9(a)).

3.3 Setup

Experiments in waveguide trapping and fluorescent imaging were done using the setup in figure 3.11. Both bright field and fluorescent experiments can be performed using this setup by removing or adding the appropriate filters. An ytterbium laser with wavelength of $1070nm$ was used as a trapping laser. After collimation it is focused on to the waveguide chip with a 100X 0.8NA objective lens. The waveguides used are strip waveguides with a strip height of $180nm$, and rib waveguides with rib height of $50nm$ and a total height of $180nm - 200nm$. Both waveguides are $1.3\mu m$ wide. Figure 3.2 show cross-sections of the two geometries. The particles are held in distilled water in a micro-chamber made of PDMS on top of the waveguide chip. For fluorescence imaging, a laser with a wavelength of 532nm is used to excite fluorescence from the top. A bandpass filter rejects the 532nm and only lets through the fluorescent signal to be captured by the CCD camera. For all the experiments on fluorescent particles, the 50X objective lens was used to acquire the images. 4X and 20X were only used for coupling and overview images. For bright field experiments both 20X and 50X were used to acquire images. The following list contain all equipment used during the experiments:

- Upright microscope
- Objective lenses of resolution 4X, 20X and 50X. The 50X objective lens has a long working distance.
- Olympus Mplan FLN 0.8NA 50X objective lens for fluorescent imaging.
- Single-mode 1070 nm ytterbium fiber laser for trapping, used at maximum $1W$.
- 100X 0.8NA IR objective lens for coupling the laser on to the waveguide.
- Cobolt Samba 532nm laser (max 1W), used to excite fluorescence.
- Vacuum holder.
- Piezoelectric translation stage from Melles Griot, model 17MDZ001.
- Manual (x,y,z) translation stage.
- Jena piezoelectric translation stage NV40/1 CLE with Labview controller.
- Different power-meters, cables, filters and accessories.
- CCD usb camera.
- Computer with software to view and record images/movies from CCD camera.

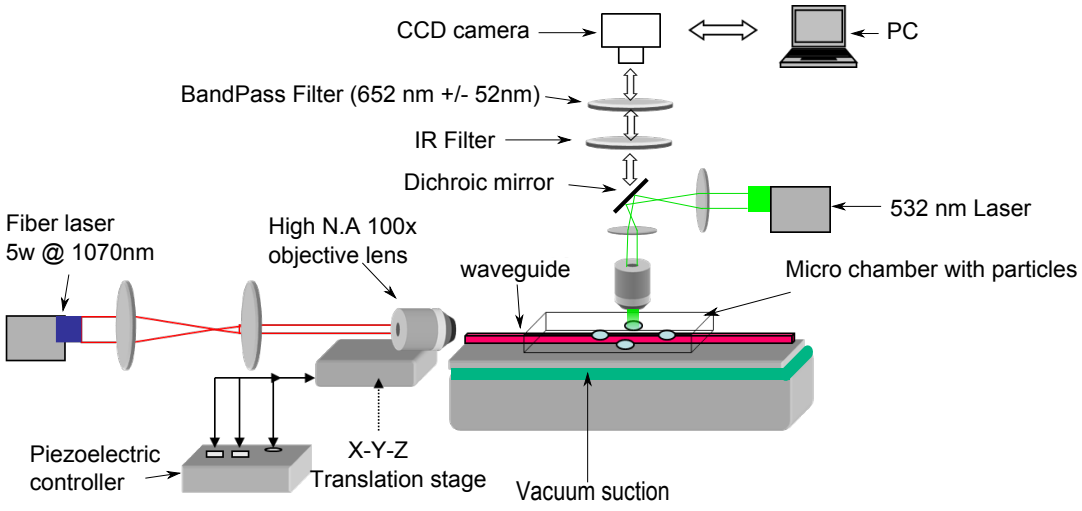

FIGURE 3.11: Setup for fluorescence microscopy integrated with waveguide trapping. Figure adapted from [17].

- Microparticles from Bang laboratories.
- Fluorescent microparticles from Bang laboratories and Phosphorex.
- Tantalum Pentoxide strip waveguides of $180nm$ strip height and $1.3\mu m$ wide.
- Tantalum Pentoxide rib waveguides of $50nm$ rib height and $1.3\mu m$ wide.
- Vacuumbrand 3000-series vacuum pumping unit and Binder vacuum oven, for preparing PDMS.
- Software for analyzing movies/images: Matlab and ImageJ/Fiji.

The experiments were conducted with both normal and fluorescent polystyrene particles of different sizes. The samples were prepared by mixing microparticles with distilled water in centrifuge tubes. The strength of the solution depend on the size of particles. To get the correct concentration, $2\mu l$ of particle solution was mixed with $1.25ml$ distilled water. The solution was then diluted one or several times depending on the desired particle concentration. For tracking of fluorescent microparticles the concentration needed to be very low to reduce noise generated by other fluorescent particles.

The waveguide chip was prepared by carefully washing it in acetone, ethanol, isoproponol and water. If the waveguide chip was very dirty, or was difficult to clean using solvents, a detergent was used. A 5% Hellermax solution was made, and the waveguide chip was submerged in the solution at 70° for 10 minutes. The results of using this cleaning method is seen in figure 3.12 where we see that the Hellermax solution makes the chip clean. It was necessary to clean the chip with a solvent to remove excess detergent from

the chip afterward. To hold the sample solution during experiments, a PDMS chamber was fabricated. 10 parts of PDMS were mixed with one part curing agent. A vacuum chamber was used to remove all air bubbles from the PDMS. The PDMS was smeared out onto a glass petri dish. The ideal PDMS layer should be as thin as possible, but a compromise between thickness and strength was needed. The thickness of the PDMS layer for this purpose ended up around $400\mu m$. The petri dish was heated on $70°C$ for 30 minutes, or until the PDMS was completely cured. A scalpel was used to cut small chambers for mounting on top of the waveguide. In an attempt to improve the image quality a thin layer of PDMS was made using a spin coater, but this became to fragile to handle.

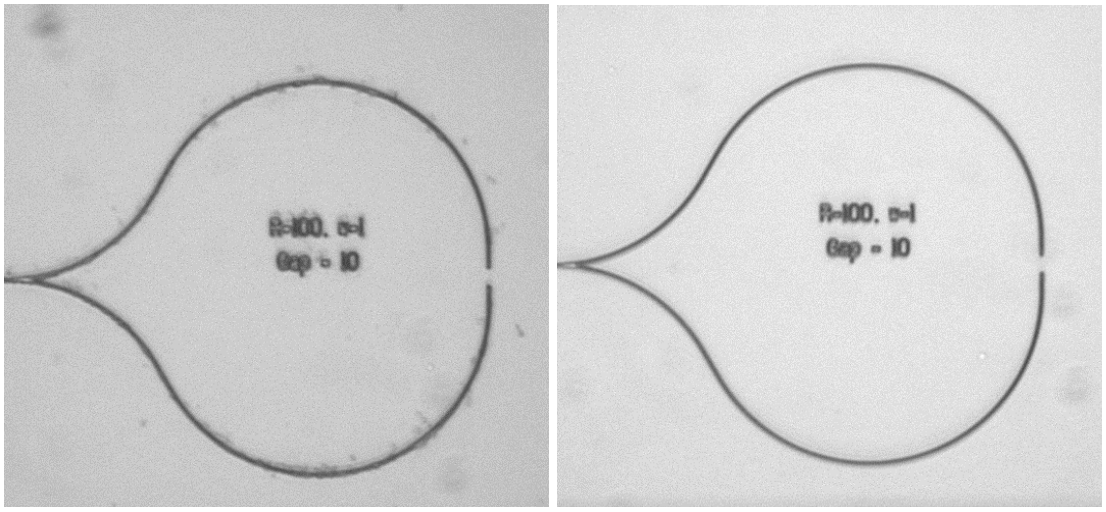

(a) Waveguide washed in isoproponol and water (b) The same waveguide after using Hellermax

FIGURE 3.12: The same waveguide chip before and after washing with Hellermax solution.

3.3.1 Approach for waveguide trapping

To enable efficient waveguide trapping of microparticles the coupling between the input laser ($1070nm$) and the waveguide chip needed to be good. The waveguide thickness was only $180nm - 200nm$, and to couple the light on to a small target like this using the objective lens was challenging. The setup was carefully aligned several times during the months of experimentation. To align the beam with the waveguide chip, the laser first need to be completely collimated and straight. This is accomplished by measuring the beam width and straightness at distances up to 1.5 meters from the source. Burning of waveguides was an apparent problem, which was only partially solved by leveling the equipment. The burning of waveguides has several other reasons, e.g stuck nanoparticles, unclean surfaces, and absorption losses inside the waveguide.

As part of the experimental training, trapping of particles both on rib and strip waveguides was performed. Trapping of microparticles can be a tedious process. After aligning the equipment as described above the laser should be focused into a small spot. The spot should ideally have the approximate size of the waveguide, but this is not possible due to the rectangular nature of the waveguides. By moving the input stage longitudinal axis and the sample stage vertical and horizontal axis, the focused spot is aligned with the waveguide. Using an infrared sensor card, a diffraction pattern is visible when the coupling is approaching the right spot. Using dark field setting on the microscope it is possible to see the spot on the computer screen. The coupling is inspected as good when there is significant scattering throughout the entire waveguide. Figure 3.13 show a 4X dark field image of a waveguide loop with a gap, where the coupling is inspected as good. In the figure we see two points along the waveguide that stands out with significantly more scattering than the surrounding waveguide. These spots should be recognized as possible hotspots. A hotspot is a defect in the structure of the waveguide caused either by fabrication error or wear and tear. The scattering from the hotspots may cause the gradient force experienced by the particle to supersede the forward pushing scattering force (with reference to figure 2.8(b)), thus particles may be trapped at the hotspot causing no particles to escape past this point. The problem of hotspots was significant and many waveguides were found unusable due to this problem.

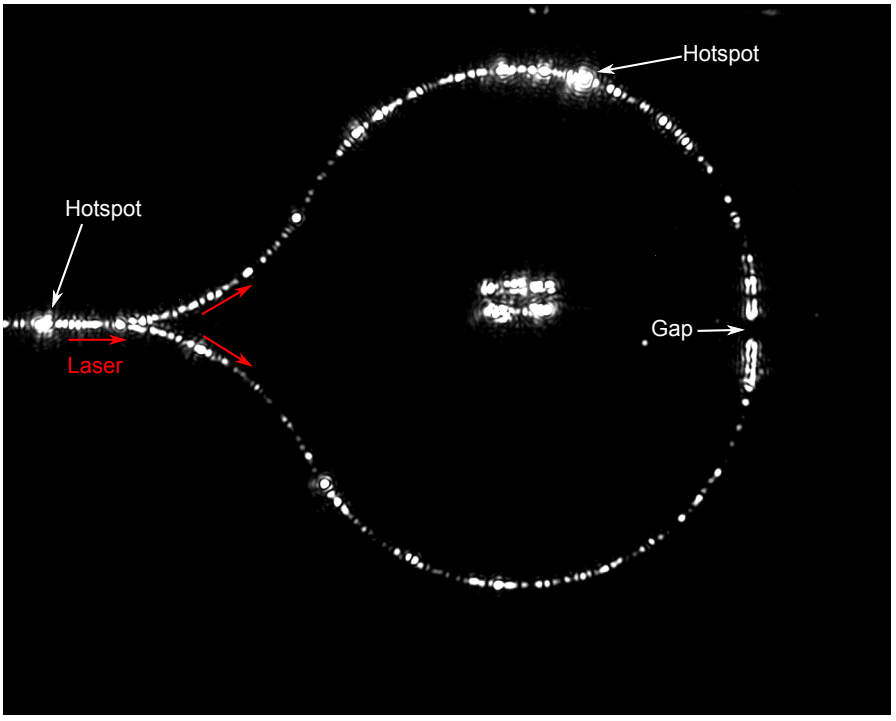

FIGURE 3.13: Good coupling in a waveguide. We see considerable scattering. In this image we also identify hotspots which might cause a problem for particles getting passed them.

When the coupling is inspected as good, particles are dropped on top of the chip with a pipette and the coverslip is put in place. The addition of a coverslip might cause the coupling to go a bit of, so a secondary maximization of the alignment is performed after putting the coverslip on.

Chapter 4

Tracking of particles on strip waveguides

This chapter gives the results after tracking fluorescent particles on strip waveguides. Section 4.1 show the results of calibrating the microscopy setup for use with the algorithm described in section 3.2. Calibration for 3 different sizes of particles is performed. Stability measurements of the setup are given in section 4.2. Results from tracking different sizes of particles on straight waveguides are given in section 4.3, and the results after tracking particles in the gap of a waveguide loop are given in section 4.4.

The error-handling during these experiments is of an important factor, as accumulated errors in some part of the measurement will impact the results coming out of the algorithm. Measurement errors, and error propagation are handled according Taylor [36]. For all the calibration series (section 4.1) in this chapter the error propagation through functions is handled as follows:

For a general function $f(x, ..., z)$ of several variables, errors $\delta_x, ..., \delta_z$ in a measured quantity $x, ..., z$ propagates through the function by

$$\delta_{f(x,...,z)} = \sqrt{\left(\frac{\partial f}{\partial x}\delta_x\right)^2 + ... + \left(\frac{\partial f}{\partial z}\delta_z\right)^2}. \tag{4.1}$$

For the calibration curves described in section 4.1 the function is proportional to $1/x$ thus, according to equation (4.1) the error propagates through the functions with a $1/x^2$ dependence. All the measured values are evaluated by their mean, and the error stated $\sigma_{\bar{x}}$ is the standard error of the mean[36] given by

$$\sigma_{\bar{x}} = \frac{\sigma_x}{\sqrt{N}}, \tag{4.2}$$

where σ_x is the standard deviation and N is the number of measurements.

In section 4.4 the weighted average [36] is used as an increased precision measurement. If we have N measurements of a quantity $x_1, ...x_N$, with individual uncertainties $\sigma_1, ...\sigma_N$, the best estimate based on these measurements is the weighted average

$$x_w = \frac{\sum_{i=1}^{N} w_i x_i}{\sum_{i=1}^{N} w_i}. \tag{4.3}$$

The weights w_i are defined as

$$w_i = \frac{1}{\sigma_i^2}, \tag{4.4}$$

for $i = 1, ...N$. The weighted average is a function of the measured quantities $x_1, ...x_N$ so the error σ_w in x_w follow the error propagation rules stated in equation (4.1), and thus becomes

$$\sigma_w = \frac{1}{\sqrt{\sum_{i=1}^{N} w_i}}. \tag{4.5}$$

When particle size is referred to in the next sections, the size of the particle is to be understood as the diameter of a uniform sphere. A $1\mu m$ big particle is thus understood as being a uniform sphere having a diameter of $1\mu m$.

4.1 Calibration

A calibration was made to map the change in vertical displacement to a change in the radius of the outermost diffraction ring. Calibration curves were made for fluorescent particles of 3 different diameters, which will be used in the waveguide trapping experiments. The calibration curves were made by imaging a particle at a distance from focus with a radius r_0 of the outermost diffraction ring, and decrease the distance from focus by steps of $1\mu m$ taking an image for each step. Figure 4.1 show some images taken from a calibration series. The calibration curve is the radius of the diffraction ring plotted against the distance from focus as seen in figure 4.2. The slope of a straight line fit through the measurements is used to map from change in diffraction ring radius to vertical displacement.

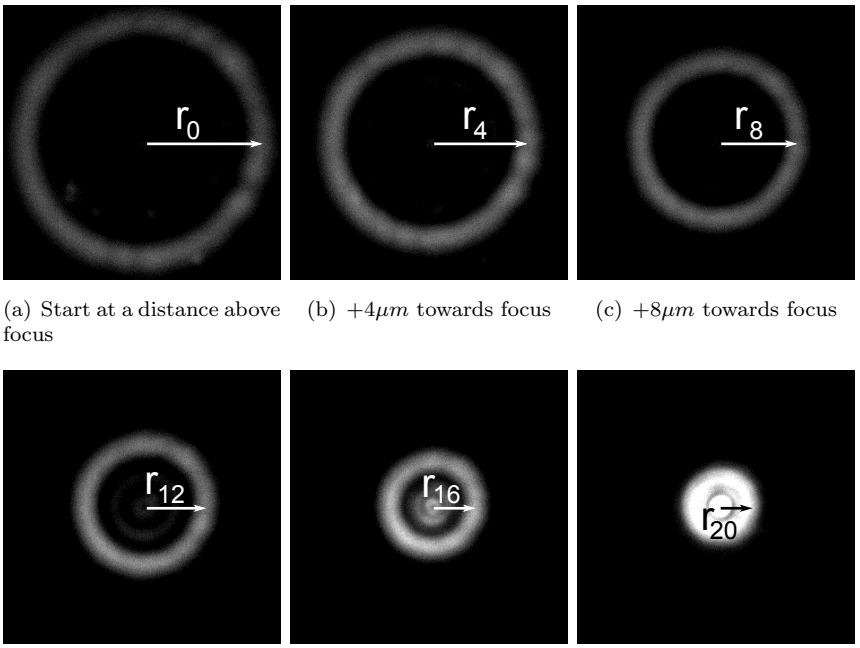

(a) Start at a distance above focus (b) $+4\mu m$ towards focus (c) $+8\mu m$ towards focus

(d) $+12\mu m$ towards focus (e) $+16\mu m$ towards focus (f) $+20\mu m$ towards focus

FIGURE 4.1: Calibration: Images taken of immobilized particle, changing the distance from focus by $1\mu m$ between every image. The radius of the outermost diffraction ring is recorded in each image and compared to the change in distance from focus.

4.1.1 Calibration for 1 μm big particles

Figure 4.2 show one of the calibration curves for $1\mu m$ big particles. The result from 10 series of calibrations done by analyzing 10 series of images taken of different $1\mu m$ big particles are shown in table 4.1. The average slope of the 10 series was $4.78px/\mu m$, meaning that a change in 1 pixel of the outermost diffraction ring corresponds to a change in vertical displacement of $\Delta z = \underline{209nm \pm 4.87nm}$, where we have used that $\Delta z = \frac{1}{slope}$.

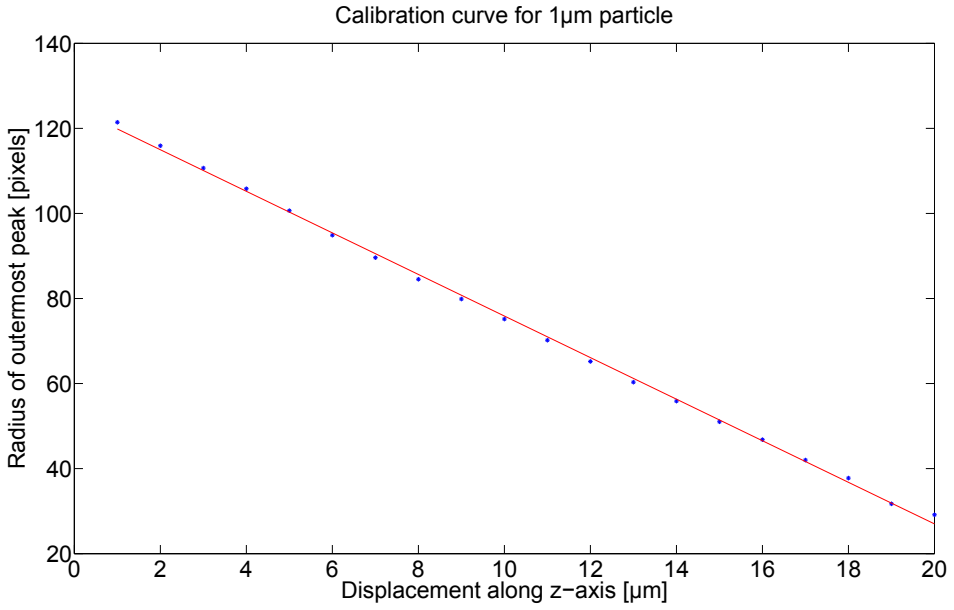

FIGURE 4.2: Calibration curve for a $1\mu m$ big particle. A series of images are taken of an immobilized particle. Between each image the distance from focus is changed by $1\mu m$. The calibration curve is thus the radius of the outermost diffraction ring as a function of the distance from focus. The equation of the straight line fit is $z = -4.89px/\mu m + 125$, and can be used to map from change in radius of the outermost diffraction ring to change in vertical displacement

TABLE 4.1: Individual slopes of 10 different calibration series for $1\mu m$ big particles, i.e 10 different readings like the one shown in figure 4.2. The average slope is used to find how much vertical displacement a change in one pixel in the outermost diffraction ring corresponds to.

	Slope $(px/\mu m)$
Series 1	4.25
Series 2	4.34
Series 3	4.42
Series 4	4.58
Series 5	4.89
Series 6	5.09
Series 7	5.03
Series 8	4.94
Series 9	5.16
Series 10	5.10
Average	4.78 ± 0.110

4.1.2 Calibration for 2 μm big particles

10 series of images were taken of $2\mu m$ big particles. The results of the calibration is given in table 4.2 where the average of these measurements gives that a change of one pixel in the radius of the outermost diffraction ring corresponds to a change in vertical displacement of $\Delta z = \underline{184nm \pm 5.79nm}$

TABLE 4.2: Individual slope of 10 different calibration series for $2\mu m$ big particles, i.e 10 different readings like the one shown in figure 4.2. The average slope is used to find how much vertical displacement a change in one pixel in the outermost diffraction ring corresponds to.

	Slope ($\mu m/px$)
Series 1	5.66
Series 2	5.73
Series 3	6.33
Series 4	4.32
Series 5	5.28
Series 6	5.61
Series 7	5.17
Series 8	5.88
Series 9	5.04
Series 10	5.45
Average	5.45 ± 0.172

4.1.3 Calibration for 3.87 μm big particles

The calibration series for 3.87 μm big particles gives that a change of 1 pixel in the radius of the outermost diffraction ring corresponds to an average vertical displacement of $\Delta z = \underline{169nm \pm 1.92nm}$. The result of the calibration is seen in table 4.3.

TABLE 4.3: Individual slope of 10 different calibration series for $3.87\mu m$ big particles, i.e 10 different readings like the one shown in figure 4.2. The average slope is used to find how much vertical displacement a change in one pixel in the outermost diffraction ring corresponds to.

	Slope ($\mu m/px$)
Series 1	5.65
Series 2	5.68
Series 3	5.64
Series 4	5.74
Series 5	6.07
Series 6	6.09
Series 7	6.19
Series 8	6.09
Series 9	6.02
Series 10	5.92
Average	5.91 ± 0.0670

4.1.4 Calibration in the horizontal plane

To determine how much distance one pixel corresponds to in the horizontal(xy) plane, a series of bright field images of particles stuck on a waveguide chip were acquired. For each image the camera was moved by a constant amount of $10\mu m$ as shown in figure 3.10. 10 measurements were done of the distance (in pixels) between each image. The average of these distances is used to calculate the one-pixel correspondence. The results of the measurement are seen in table 4.4 where we see 10 distances measured in pixels. Dividing $10\mu m$ by their average gives us the answer, and the error is found by error propagation rules stated in eq.(4.1). The final result of the calibration gives that a change in one pixel in the xy-plane corresponds to $\Delta xy = \underline{66.4nm \pm 0.62nm}$.

4.1.5 Summary calibration

The results of calibrating for different sizes of particles are summarized in table 4.5. A change in 1 pixel of the outermost diffraction ring maps with an inverse relation to particle diameter. It should be noted that all the calibrations were done using the same 50X 0.8NA objective lens. This is the same lens used for all the fluorescence imaging experiments. If we were to introduce another objective lens, the calibration must be repeated using this lens.

TABLE 4.4: Distances in pixels between immobilized particles as shown in figure 3.10. Each measurement is based on two still images, where the camera is moved by $10\mu m$ between each image. The distance between a particle in one image and the same particle in the next image is then measured. The average distance is used to determine the size (in nm) of one pixel for the 50X 0.8NA objective lens used during the experiments.

Measurement	Distance in pixels
1	142.1
2	155.3
3	149.2
4	153.3
5	150.2
6	144.2
7	155.1
8	151.1
9	150.3
10	154.2
Average	150.5 ± 1.41

TABLE 4.5: Summary of the calibration. Vertical mapping is the amount of vertical displacement when the outermost diffraction ring changes with 1 pixel. We also see the size of one pixel in the horizontal plane.

Particle diameter	Vertical mapping	Size of 1 pixel in xy plane
$1\mu m$	$209nm \pm 4.87nm$	$66.4nm \pm 0.62nm$
$2\mu m$	$184nm \pm 5.79nm$	$66.4nm \pm 0.62nm$
$3.87\mu m$	$169nm \pm 1.92nm$	$66.4nm \pm 0.62nm$

4.2 Stability test of the setup

To quantify the error contributed by the method, the stability of the setup must be known. The stability of the setup can be found by repeating the same experiment over time, and analyzing the result. To achieve this, 5 Movies of 19.5 seconds each were captured of immobilized particles slightly out of focus such that the diffraction rings were visible. Each movie consist of 150 frames. During the length of the movies the particles photo-bleached so that the intensity of the rings became gradually weaker. The movies were analyzed frame by frame to reveal information about the stability of the setup. The maximum relative displacement of the center in both y,- and x direction is seen in table 4.6 as δ_{cy} and δ_{cx}. An estimate for the maximum error in tracking the center of a particle during the length of the movies can then be an average of the 5 measurements, i.e $\bar{\delta}_{cy} = \underline{170nm}$ and $\bar{\delta}_{cx} = \underline{162nm}$.

To investigate the vertical drift of the setup, the vertical displacement of the particle was tracked through the same 5 movies. σ_z in table 4.7 is the standard deviation of a straight line fit through the vertical displacement measurements. The maximum vertical displacement, i.e the maximum peak-to-peak value in the vertical displacement

measurement, is given by δz_{max}. An error $\bar{\sigma}_{z(error)}$ associated with both the mechanical drift, photo-bleaching and algorithm can then be an average of the individual standard deviations; $\bar{\sigma}_{z(error)} = \underline{50.2nm}$.

Figure 4.3(a) show the vertical displacement of a particle during one of the stability tests. Figure 4.3(b) show the average intensity of each frame in the movie. We clearly see the downward slope in both figures, i.e the reduction in intensity due to photo-bleaching will make the particle appear to move down.

The linear trend in figure 4.3(a) and 4.3(b) caused by photo-bleaching and slowly varying mechanical drift can be accounted for by subtracting a linear fit from the data-sets (this will be referred to as *detrending* the data-set). Doing this to the vertical displacement in figure 4.3(a) we get figure 4.3(c). The remaining noise in figure 4.3(c) must then be algorithm noise and fast varying mechanical noise, i.e vibrations. To see the impact of removing linear trends from this data, the maximum error δz_{max} before and after detrending the 5 data-sets is shown in table 4.7. The average maximum error improves by 28.7% after detrending the data-set.

For the experiments in the next sections improvements were made to reduce the photo-bleaching, but other linear trends caused by angles in the setup can cause similar situations that can be accounted for by detrending the data.

TABLE 4.6: Individual readings of the maximum horizontal plane drift in both the y-direction δ_{cy} and x-direction δ_{cx} for immobilized particles imaged over 19.5 seconds each.

Test	δ_{cy}	δ_{cx}
1	105nm	94.0
2	252nm	241nm
3	207nm	220nm
4	80.5nm	107nm
5	205nm	150nm

TABLE 4.7: Individual standard deviations σ_z of a straight line fit of the vertical displacement of a particle during 5 stability test. We also see the maximum peak-to-peak values δz_{max} both before and after (last column) linear trends have been removed.

Test	σ_z	δz_{max}	δz_{max} after detrend
1	32.7nm	223nm	207nm
2	58.7nm	448nm	290nm
3	49.6nm	278nm	263nm
4	43.5nm	407nm	238nm
5	66.4nm	665nm	442nm

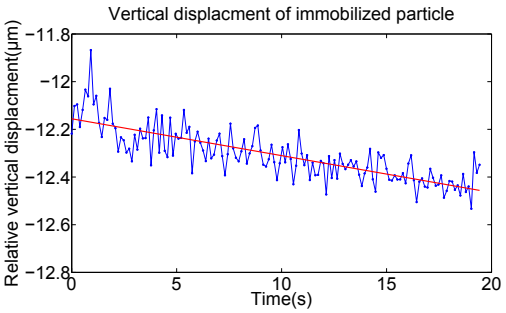

(a) Vertical displacement as function of time for a particle stuck on the waveguide chip

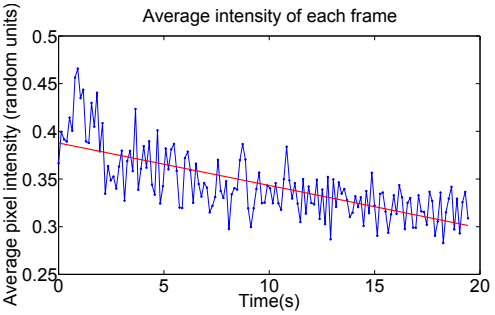

(b) Average intensity in each frame of the movie

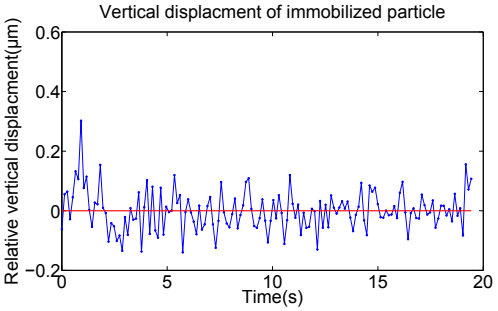

(c) Vertical displacement after linear trends have been removed

FIGURE 4.3: Immobilized particle imaged over 19.5 seconds. We see linear trends in both the average intensity of the frames (b) and the vertical displacement (a) of the particle. (c) Show the vertical displacement after the trend has been removed

4.3 Tracking of particles propelling on a straight waveguide

In this section we study the vertical motion of particles as they propel on straight waveguides. The particles are tracked using the algorithm described in section 3.2 together with off-focus movies of the fluorescent particles. Horizontal tracking is also performed by following the center of the particles. The particles used are fluorescent polystyrene spheres with a diameter of $1\mu m$, $2\mu m$ and $3.87\mu m$. Particles of diameter $500nm$ were also tried, but the poor fluorescent signal they produced became impossible to image properly as they propelled on the waveguides. The result of tracking $500nm$ big particles are thus not included in this thesis.

4.3.1 3D tracking of $1\mu m$ big particles on a straight waveguide

Off focus movies of fluorescent particles with a diameter of $1\mu m$ were captured as the particles propelled on a straight waveguide. The movies were imported into Matlab

where each frame were analyzed using the algorithm described earlier. The particles were tracked in both the vertical and horizontal plane. Many movies were acquired, and the 10 best movies were analyzed. **Movie 4** shows one example of a movie acquired. The outermost diffraction ring of the particle is tracked through the entire movie.

The relative vertical displacement for each frame in the movie is recorded by the algorithm. The standard deviation of a straight line fit through the vertical displacement measurements is recorded for every movie analyzed, which is shown in table 4.8. This gives an average standard deviation of $\bar{\sigma}_z = \underline{62.6nm \pm 6.35nm}$. The maximum relative vertical displacement δz_{max} is recorded in the second column of table 4.8 where we see an average of $\delta \bar{z}_{max} = \underline{301nm \pm 32.9nm}$. After removing linear trends the average maximum relative displacement became a bit smaller; $\delta \bar{z}_{max} = \underline{292nm \pm 38.7nm}$. The linear trends are believed to come from angles in the setup and photo-bleaching of the particles.

Figure 4.4(a) show the result from the vertical tracking of a particle moving on a straight waveguide. From figure 4.4(b) we notice that the fluorescent signal is corrupted by noise as the particle passes what is believed to be spots of dirt on the CCD chip. This is seen in frames 38 and 117 in figure 4.4(b), where we notice the impact on the vertical displacement in figure 4.4(a) as the diffraction ring becomes corrupted by noise. Both the detection of the center and the radius of the estimated diffraction ring change as the dust particle passes through the ring. For this particular movie the frames that contained the most amount of noise were removed to obtain a more precise result. The standard deviation of the vertical displacement of the particle improved from $64.4nm$ to $55.6nm$. Figure 4.4(c) show the transverse (y-direction) tracking of the particle. The particle is meandering which is a result of intensity beating between the modes in the waveguide. The waveguide is thus supporting multiple modes. Figure 4.4(b) show the relative longitudinal (x-direction) position of the center for the selected frames.

TABLE 4.8: Results from tracking the vertical displacement of $1\mu m$ big particles on straight waveguides. σ_z is the individuals standard deviations of the vertical displacement. We also see the maximum vertical displacement δz_{max} both before and after linear trends have been removed.

	σ_z	δz_{max}	δz_{max} after detrend
Movie 1	59.3nm	289 nm	243nm
Movie 2	76.8nm	280nm	276nm
Movie 3	64.4nm	380nm	422nm
Movie 4	104nm	466nm	539nm
Movie 5	54.5nm	277nm	238nm
Movie 6	71.0nm	225nm	250nm
Movie 7	25.5nm	88.3nm	88.0nm
Movie 8	50.1nm	293nm	217nm
Movie 9	61.6nm	363nm	302nm
Movie 10	59.1nm	347 nm	342nm
Average	$62.6nm \pm 6.35nm$	$301nm \pm 32.9nm$	$292nm \pm 38.7$

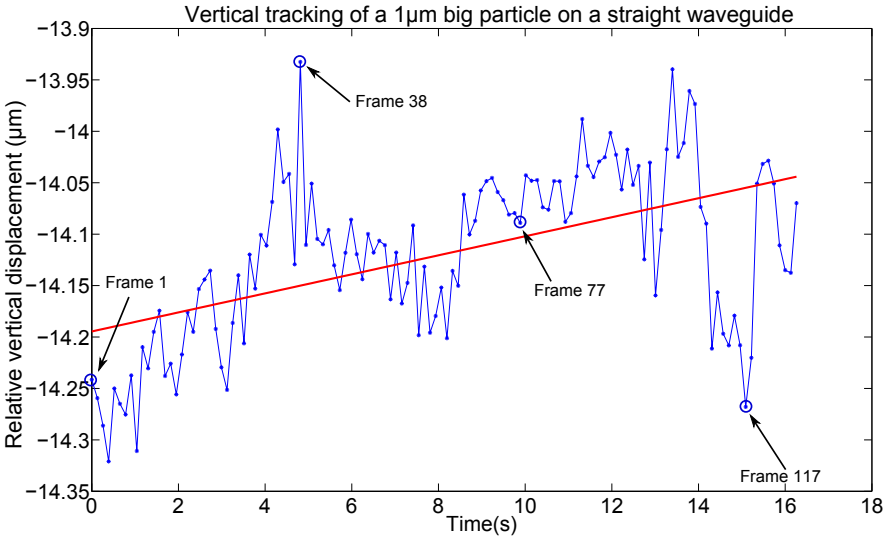

(a) Vertical tracking of a $1\mu m$ big particle.

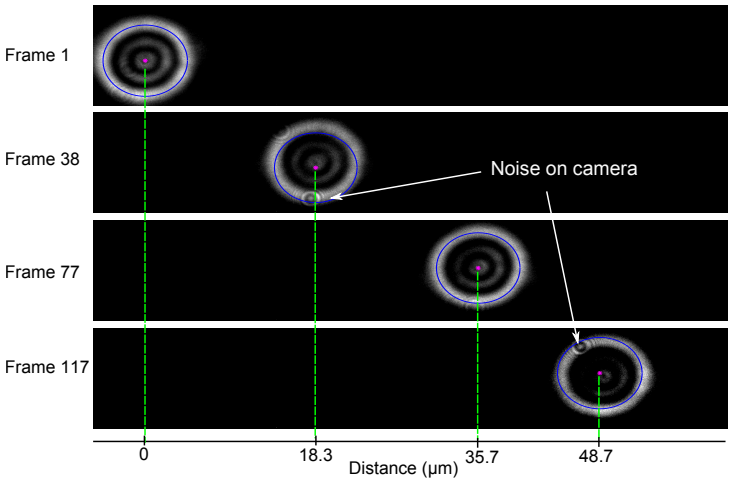

(b) 4 selected frames from the movie analyzed and the longitudinal (x-direction) position of the particle at those frames.

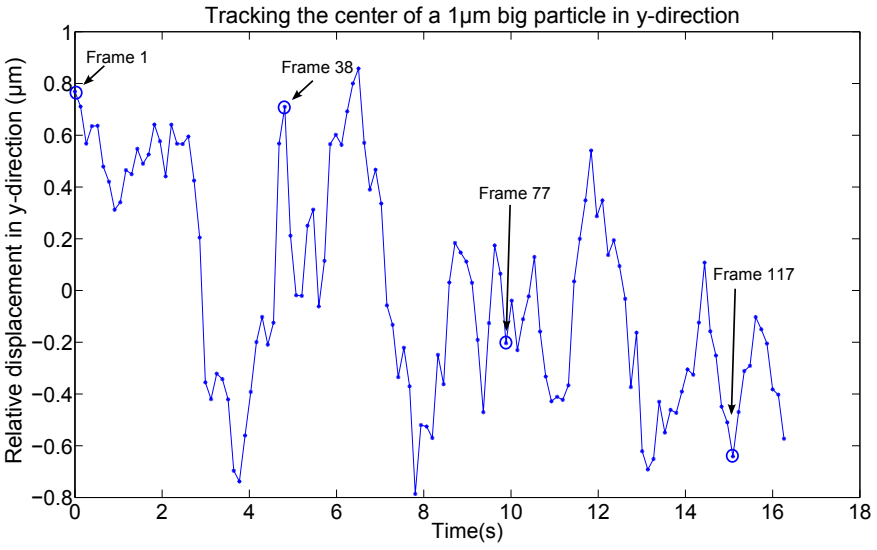

(c) Horizontal (y-direction) tracking of the same particle centered around its mean value

FIGURE 4.4: Tracking of a $1\mu m$ big particle on a straight waveguide. (a) The vertical displacement of the particles is tracked trough all the frames of the movie. (b) Show some frames taken from the movie as the particle is propelling forwards. (c) Show the transverse (y-direction) tracking where we see meandering of the particle indicating higher order modes.

4.3.2 3D tracking of 2μm big particles on a straight waveguide

10 movies were captured of 2μm big particles propelling on a straight waveguide. The result of the vertical tracking can be seen in table 4.9 where we see the 10 standard deviations σ_z from a linear fit for each measurement. Figure 4.5(a) shows the vertical tracking of one particle. The diffraction rings with their corresponding radius can be seen in figure 4.5(b) where we also see the longitudinal (x-direction) position of the center of the particles for those frames. Figure 4.5(c) show the transverse (y-direction) tracking where we notice that the particle is meandering. The vertical displacement of the particles has an average standard deviation of $\bar{\sigma}_z = \underline{54.6nm \pm 2.83nm}$. The maximum peak to peak value δz_{max} of the vertical displacement is also shown in table 4.9 both before and after linear trends have been removed. The average maximum peak to peak value was found to be $\delta z_{max} = \underline{256nm \pm 13.8nm}$ after detrending. It can be noticed from figures 4.5(a) and 4.5(b) that frame number 28 is very bright and also shows relatively high vertical displacement. Non-uniformity of the laser used for exciting fluorescence is believed to cause the frame to appear bright.

TABLE 4.9: Results from tracking the vertical displacement of 2μm big particles on straight waveguides. σ_z is the individuals standard deviations of the vertical displacement. We also see the maximum vertical displacement δz_{max} both before and after linear trends have been removed.

	σ_z	δz_{max}	δz_{max} after detrend
Movie 1	51.3nm	345 nm	235nm
Movie 2	44.8nm	256nm	275nm
Movie 3	49.7nm	286nm	294nm
Movie 4	49.3nm	224nm	218nm
Movie 5	62.8nm	296nm	281nm
Movie 6	59.8nm	287nm	248nm
Movie 7	49.8nm	327nm	281nm
Movie 8	42.7nm	182nm	166nm
Movie 9	70.9nm	325nm	317nm
Movie 10	61.0nm	246nm	241nm
Average	$54.6nm \pm 2.83nm$	$277nm \pm 16.1nm$	$256nm \pm 13.8nm$

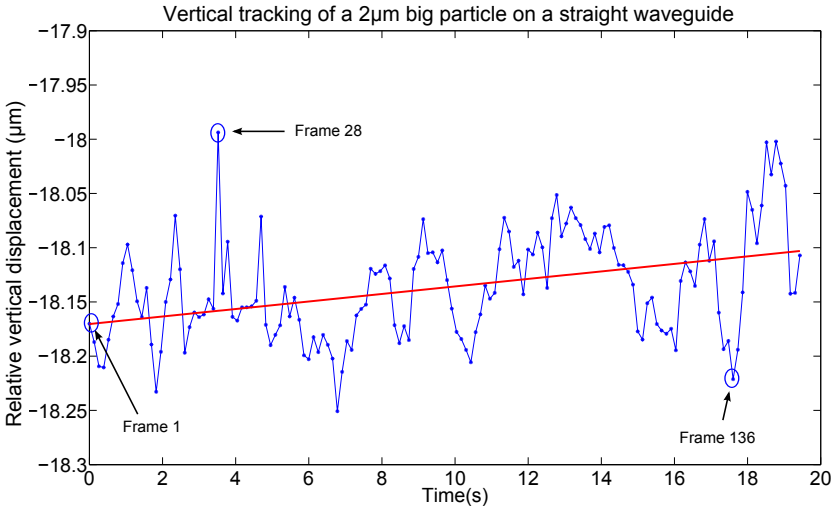

(a) Vertical tracking of a $2\mu m$ big particle.

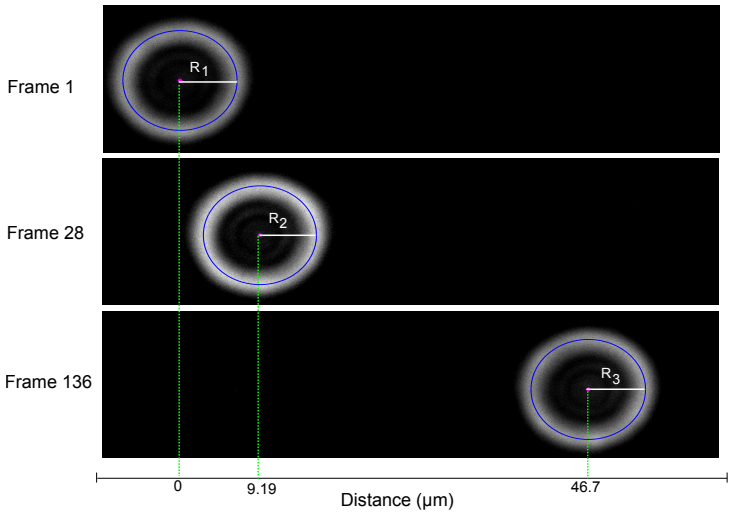

(b) 3 selected frames from the movie analyzed and the longitudinal (x-direction) position of the particle at those frames.

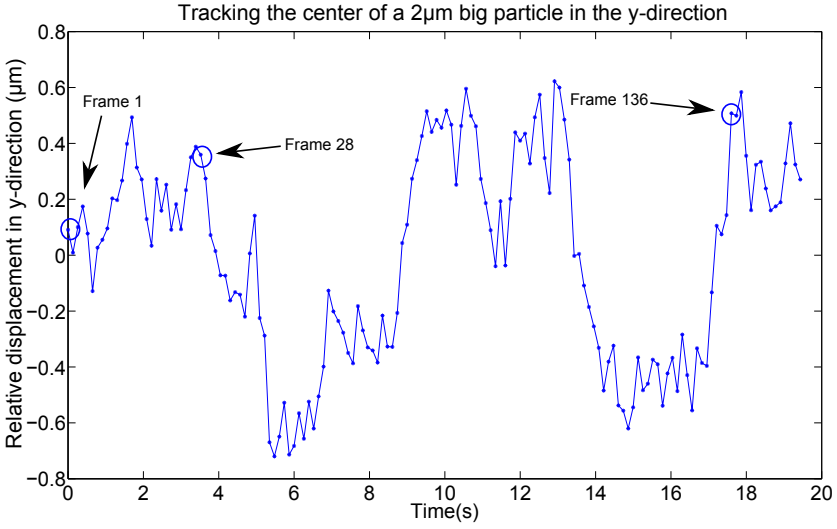

(c) Show horizontal (y-direction) tracking of the particle.

FIGURE 4.5: Tracking of a $2\mu m$ big particle on a straight waveguide. (a) The vertical displacement of the particles is tracked trough all the frames of the movie. (b) Show some frames taken from the movie as the particle is propelling forwards and also show the longitudinal (x-direction) tracking of the particle. (c) Show the transverse (y-direction) tracking where we see meandering of the particle indicating higher order modes.

4.3.3 Vertical tracking of 3.87μm big particles on a straight waveguide

4 movies were analyzed of 3.87μm big particles propelling on a straight waveguide. The standard deviations σ_z of a straight line fit are seen in table 4.10. The average standard deviation $\bar{\sigma}_z = \underline{85.2 \pm 9.38nm}$ describes the vertical motion of the particles as they propel along the waveguide. The maximum vertical displacement δz_{max} is also seen in table 4.10, where we see that after removing linear trends the average maximum relative vertical displacement is $\delta \bar{z}_{max} = \underline{393nm \pm 53.2}$.

TABLE 4.10: Results from vertical tracking of 3.87μm big particles on straight waveguides. σ_z is the standard deviation of a straight line fit. We also see the maximum vertical displacement δz_{max} both before and after linear trends have been removed.

	σ_z	δz_{max}	δz_{max} after detrend
Movie 1	110nm	665 nm	451nm
Movie 2	74.1nm	525nm	318nm
Movie 3	67.8nm	553nm	289nm
Movie 4	89.0nm	947nm	512nm
Average	$85.2 \pm 9.38nm$	$673nm \pm 96.4nm$	$393nm \pm 53.2nm$

4.4 Tracking of particles in the gap of a strip waveguide loop with a gap separation of 10μm

For a strip waveguide loop with a gap separation of 10μm, the counter diverging fields from the waveguide ends have been simulated, by O.G Hellesø, to create trapping locations that are above the waveguide chip. Figure 3.6(b) show the simulated vertical (z-direction) force where we see the force turn positive at some point along the gap thus indicating levitation. Figure 3.6(c) show the simulated horizontal (x-direction) force, i.e along the gap. From the figure we see the force oscillating creating several positions where a restoring force is present. A series of experiments were conducted in attempt to confirm the hypothesis of vertical displacement in the gap of a strip waveguide loop. Movies were taken of particles of different sizes as they are trapped in the gap on a strip waveguide loop. The vertical displacement is measured with reference to the average vertical position of the particle as it propels towards the gap. The particle moves on the waveguide as it enters the field of view with a radius of the outermost diffraction ring r_1 as seen in figure 4.6(a). As is interacts with the counter-diverging fields in the gap it levitates, which makes the radius of the outermost diffraction ring r_2 become smaller as seen in figure 4.6(b). The average difference in r_1 and r_2 will then be a measurement of how much the particle has levitated. To get the vertical distance above the waveguide chip that the particle is trapped, 180nm must be added which corresponds to the strip height.

When tracking a particle in the horizontal plane in the gap of a strip waveguide, transverse (y-direction) tracking has been left out. Tracking the center of a particle automatically give a result for both dimensions (both x- and y-direction), but the main purpose for tracking in the horizontal (xy) plane is to measure the longitudinal distance (x-direction) from the waveguide ends where the particles are trapped.

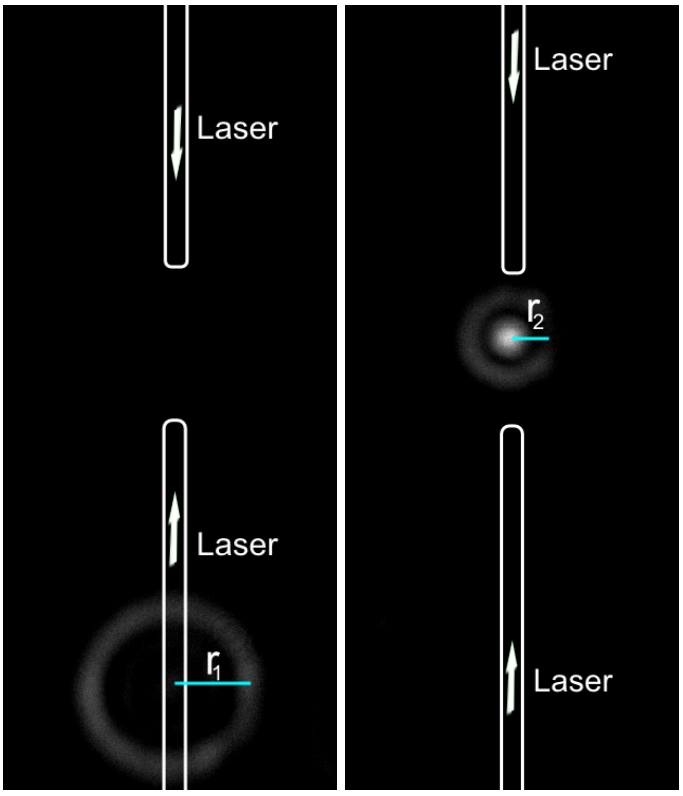

(a) Particle propelling on the straight waveguide with diffraction ring radius r_1.

(b) Particle trapped in the gap with diffraction ring radius r_2.

FIGURE 4.6: Trapping a $1\mu m$ big particle in a $10\mu m$ wide gap on a strip waveguide. The diffraction ring radius is smaller in the gap than on the loop arm which indicate levitation.

4.4.1 Vertical tracking a $1\mu m$ big particles in a 10 μm wide gap on a strip waveguide

Many movies were acquired of $1\mu m$ big particles trapped in a $10\mu m$ wide gap on strip waveguides. 7 movies were used with the algorithm to translate diffraction ring radius to vertical displacement. The trap was inspected to be weak, in that the particles were not clearly trapped but seem to wander away from the area once they had been levitated. Only one movie showed what resembled stable trapping. **Movie 5** show the movie from this particular experiment, where we see the off focus fluorescent particle entering the

gap. As it is trapped the radius of the diffraction rings clearly become smaller indicating levitation. Another particle enters the gap and knocks away the trapped particle. The vertical tracking of the trapped particle from this particular experiment as a function of time is seen in figure 4.7. The result showing the individual vertical displacement of 7 particles is seen in table 4.11. The last two rows of the table gives the average and weighted average vertical displacement, respectively. We see that the particles are levitated by $\bar{z}_w = \underline{5.63\mu m \pm 91nm}$. Noisy movies made a horizontal(xy) plane tracking difficult as the individual frames of the movies needed to be cropped to remove unwanted noise, thus also removing the reference between the frames.

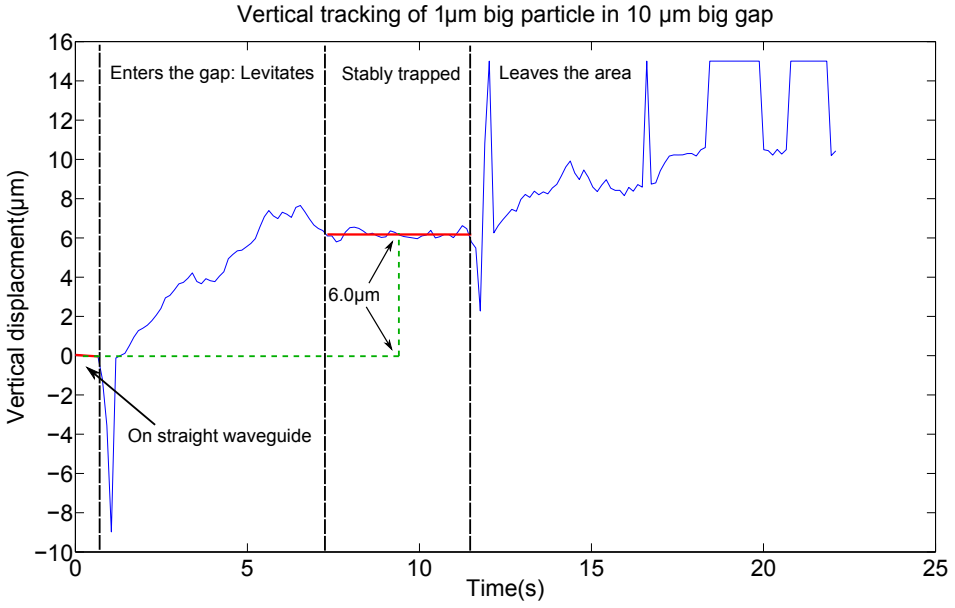

FIGURE 4.7: Vertical tracking of a $1\mu m$ big particle in a $10\mu m$ big gap on a strip waveguide. The particle is levitated $6.0\mu m$ relative to the waveguide end. Adding $180nm$ to compensate for the strip height give the levitation distance above the gap/waveguide chip. The spikes in the curve corresponds to bad frames/noise. The particle collides with another particle that enters the gap. This causes the particle to be knocked away from the gap. See **Movie 5**.

TABLE 4.11: Vertical displacement of $1\mu m$ big particles in a $10\mu m$ wide gap on strip waveguides. 180nm has been added to the vertical displacement column which corresponds to the height of the strip waveguide

	Vertical displacement
Movie 1	$4.60\mu m \pm 198nm$
Movie 2	$4.73\mu m \pm 1.07\mu m$
Movie 3	$5.93\ \mu m \pm 572nm$
Movie 4	$5.83\ \mu m \pm 859nm$
Movie 5	$3.79\ \mu m \pm 456nm$
Movie 6	$6.18\mu m \pm 213nm$
Movie 7	$5.99\ \mu m \pm 126nm$
Average	$5.29\mu m\ \pm 346nm$
Weighted average	$5.63\ \mu m \pm 91.0nm$

4.4.2 3D tracking of $2\mu m$ big particles in a 10 μm wide gap on a strip waveguide

$2\mu m$ big particles were tracked as they interacted with the 10 μm wide gap. **Movie 6** show one of the movies analyzed. Using the calibration curve for mapping the radius of the diffraction rings to vertical displacement, the particles average levitation when trapped was measured. The fluorescent signal was much better for $2\mu m$ big particles than for the smaller particles. In contrast to $1\mu m$ big particles, $2\mu m$ big particles did not need to be cropped out of the movies, thus enabling horizontal tracking. The particles were visually inspected to accelerate when entering the trap, and this is confirmed by comparing the plot of the longitudinal (relative x-position) tracking of the center with the relative vertical displacement as seen in figure 4.8. The position of the particle when the acceleration into the trap started, was used as a measure for the transition between waveguide and gap. This made it possible to pinpoint the longitudinal (x-direction) trapping location as a distance from the waveguide end. Table 4.12 show the individual results of vertical tracking of 6 particles in the gap, and their respective trapping distances from the waveguide ends. Using the weighted average, the particles levitated $\bar{z}_w = \underline{663nm \pm 76.9nm}$. The particles were trapped at a horizontal distance of $\bar{x}_w = \underline{6.54\mu m \pm 90.7nm}$ from the end of the waveguide.

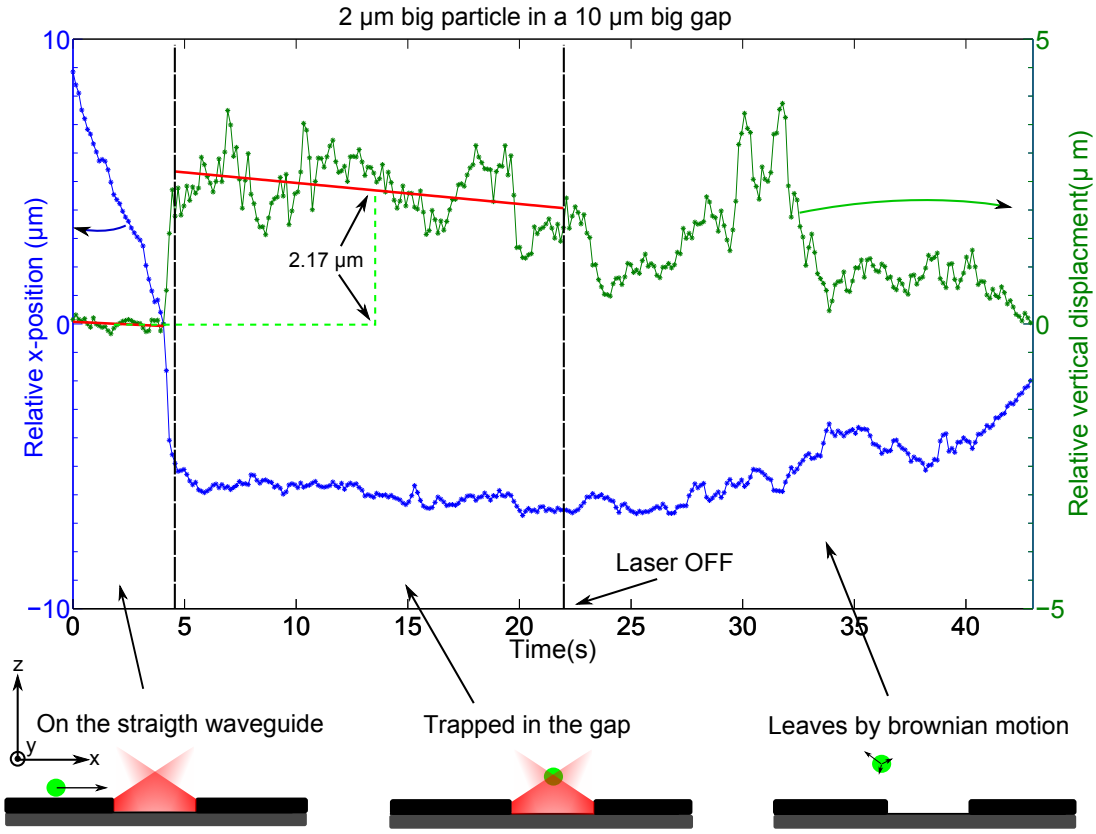

FIGURE 4.8: Vertical and longitudinal (x-direction) tracking of a $2\mu m$ big particle in a $10\mu m$ wide gap. The particle is levitated $2.17\mu m$ relative to the waveguide. Adding $180nm$ to compensate for the strip height gives the levitation distance above the waveguide chip.

TABLE 4.12: Vertical displacement of $2\mu m$ big particles in a $10\mu m$ wide gap strip waveguides, and the distance they are trapped from the waveguide ends. 180nm has been added to the vertical displacement column which corresponds to the height of the strip waveguide

	Vertical displacement	Trapping distance from end
Movie 1	522nm ±97nm	$6.38\mu m$±163nm
Movie 2	1.66 $\mu m \pm$ 462nm	$5.49\mu m$±325nm
Movie 3	810 nm ±180nm	5.09 μm± 371nm
Movie 4	787 nm ±346nm	8.23 μm± 219nm
Movie 5	2.35 μm±506nm	5.98 μm±191nm
Movie 6	533 ±260 nm	6.89 ± 230nm
Average	$1.11\mu m \pm 309nm$	$6.34\mu m \pm 250nm$
Weighted average	$663nm \pm 76.9nm$	$6.54\mu m \pm 90.7nm$

4.4.3 3D tracking of a 3.87μm big particle in a 10 μm wide gap on a strip waveguide

One movie was captured of a 3.87μm big particle in the gap of a strip waveguide loop. Its vertical displacement and longitudinal trapping location is seen in table 4.13. The particle levitated $z = \underline{317nm \pm 35nm}$, and was trapped at a horizontal (x-direction) distance of $x = \underline{5.45\mu m \pm 140nm}$.

TABLE 4.13: Vertical displacement of a 3.87μm big particle, and the trapping distance form the end in a 10μm wide gap on strip waveguides. 180nm have been added to the vertical displacement which corresponds to the height of the strip waveguide

	Vertical displacement	Trapping distance from end
Movie 1	317nm ±35nm	5.45μm±140nm

Chapter 5

Rib waveguide trapping

The strip waveguide loop is able to stably trap particles in the gap for small gap separations, i.e separations $\leq 20\mu m$. A drawback with the strip waveguide geometry is that it can only provide a stable trap for one particle. New particles entering the gap of a strip waveguide loop will knock away the particle already trapped. We saw examples of this is in figure 4.7 where a $1\mu m$ big particle knocks away a particle already trapped in a $10\mu m$ big gap. An example using a larger gap separation is seen in figure 5.1(a) where we see a $3\mu m$ big particle trapped in the gap on a strip waveguide with a gap separation of $20\mu m$. As another particle enters the gap, the particle is knocked out as seen in figure 5.1(b) and 5.1(c). The weak trap of the strip waveguide is seen to only accommodate one particle. The entire movie can be seen in **Movie 7**.

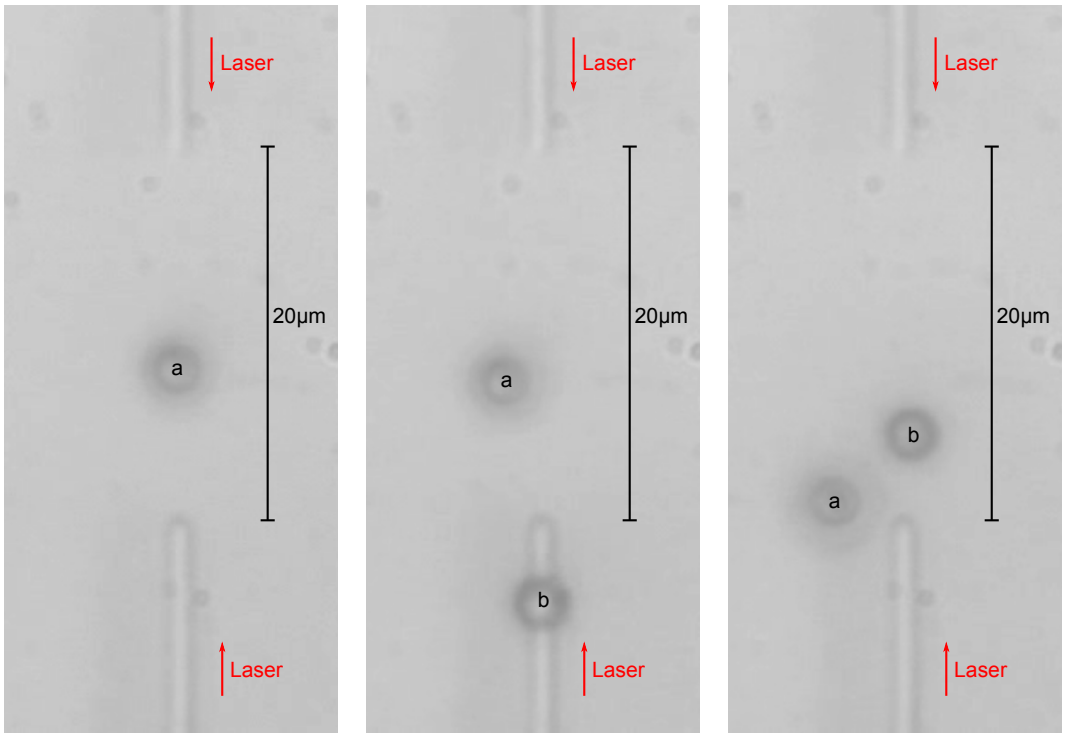

(a) Particle a is trapped in the gap.

(b) Particle b propelling towards the gap.

(c) Particle a is knocked out as particle b is trapped.

FIGURE 5.1: Trapping a $3\mu m$ particle in a $20\mu m$ wide gap on a strip waveguide. Since there is no evanescent field present in the gap,the trapping force is weak. This makes the trap unable to hold more than one particle.

The rib waveguide (figures 2.6, 3.5(b) and 3.5(d)) has a guiding medium in the gap and thus offers a downward attractive force along the entire gap. This provides a stable trap for both small and large gap separations. Particles entering a gap on a rib waveguide is attracted towards the waveguide chip by the evanescent field. The trap on the rib waveguide is thus able to accommodate more than one particle.

The horizontal (x-direction) force acting on a $3\mu m$ big particle in a $10\mu m$ big gap on a rib waveguide, has been simulated by O.G.Hellesø. The simulation can be seen in figure 5.2(a) where we see one point along the gap where a restoring force is present. This is the point where the horizontal force is zero. The restoring force holds the particle at the given location. The simulated vertical (z-direction) force is seen in figure 5.2(b) and is negative in the entire gap, i.e the particle will be attracted towards the waveguide chip. This is an important difference from the strip waveguide loop. If we consider figure 3.6(a) we saw that the vertical force in a $10\mu m$ big gap acting on a $2\mu m$ big particle on a strip waveguide, became positive at around $3.4\mu m$, thus levitating the particle. For the rib waveguide we see a negative vertical force in the gap, attracting particles towards the waveguide chip. To investigate the result from the simulation several experiments

were performed using particles of different sizes. Rib waveguides with a rib height of $50nm$ and a width of $1.3\mu m$ were used, and different loop radius and gap separations were investigated.

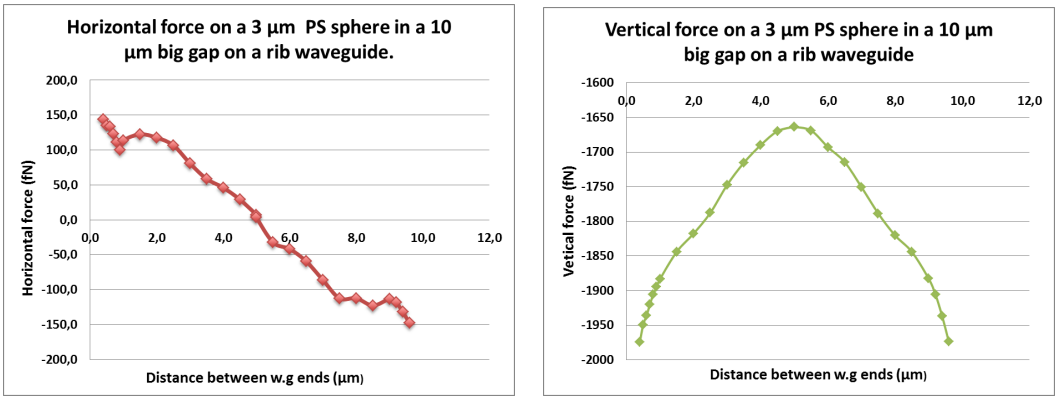

(a) Horizontal force as function of gap separation.

(b) Vertical force as function of gap separation.

FIGURE 5.2: Simulation of optical forces acting on a $3\mu m$ big particle in a $10\mu m$ wide gap on a rib waveguide.

The simulations were performed using a gap separation of $10\mu m$. The waveguides used in this thesis that offers a gap size of $10\mu m$, have a loop radius of $100\mu m$. Many attempts were performed in trying to propel particles on this rib waveguide loop, but without any success. With reference to section 2.2.3 where we discussed propagation losses, the equation that described bend-loss in a waveguide bend (eq.(2.26)) showed that the loop radius and bend-loss have an inverse exponential relationship. During the experiments, a need to increase the loop radius in order to get the particles to propel on the loop was found. The rest of the experiments on rib waveguides were thus performed with a loop radius of $200\mu m$, and gap separations of $20\mu m$ and $50\mu m$.

5.1 Trapping of $3\mu m$ big particles in the gap on rib waveguides

3 μm big particles were trapped on rib waveguides with a loop radius of $200\mu m$. Figure 5.3(a) show a particle as it is approaching a $20\mu m$ wide gap. The particle is stably trapped in the gap and another particle follow also being trapped at the same location as seen in figure 5.3(b) and 5.3(c). **Movie 8** shows the movie recorded from this experiment.

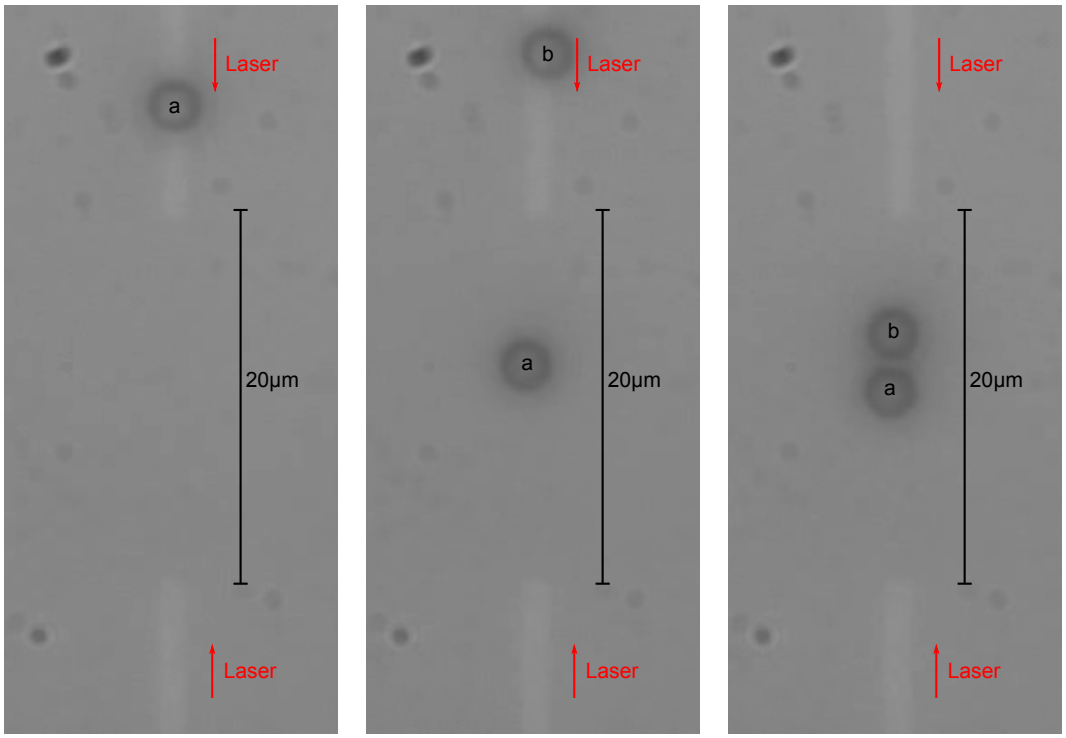

(a) Particle a is propelling towards the gap.

(b) Particle a is trapped in the gap, and particle b is propelling towards the gap.

(c) Particle a and b is both trapped in the gap.

FIGURE 5.3: Trapping a $3\mu m$ big particle in $20\mu m$ wide gap on a rib waveguide. The downward gradient force make room for more than one particle in the trap.

Several particles were trapped using a rib waveguide with gap separation of $50\mu m$ as can be seen in **Movie 9**. Figure 5.4(a) shows a frame from the movie where three particles are trapped in the gap. The particles form lines directed along the gap. When the line has sufficient number of members, the particles seem to battle for the best spots near the highest field intensity. This can be seen in figure 5.4(b) which is another frame from the movie, where the particle approaching from below pushes past the three settled particles. Parallel lines may also be formed in the case of many particles in the gap as seen in figure 5.4(c).

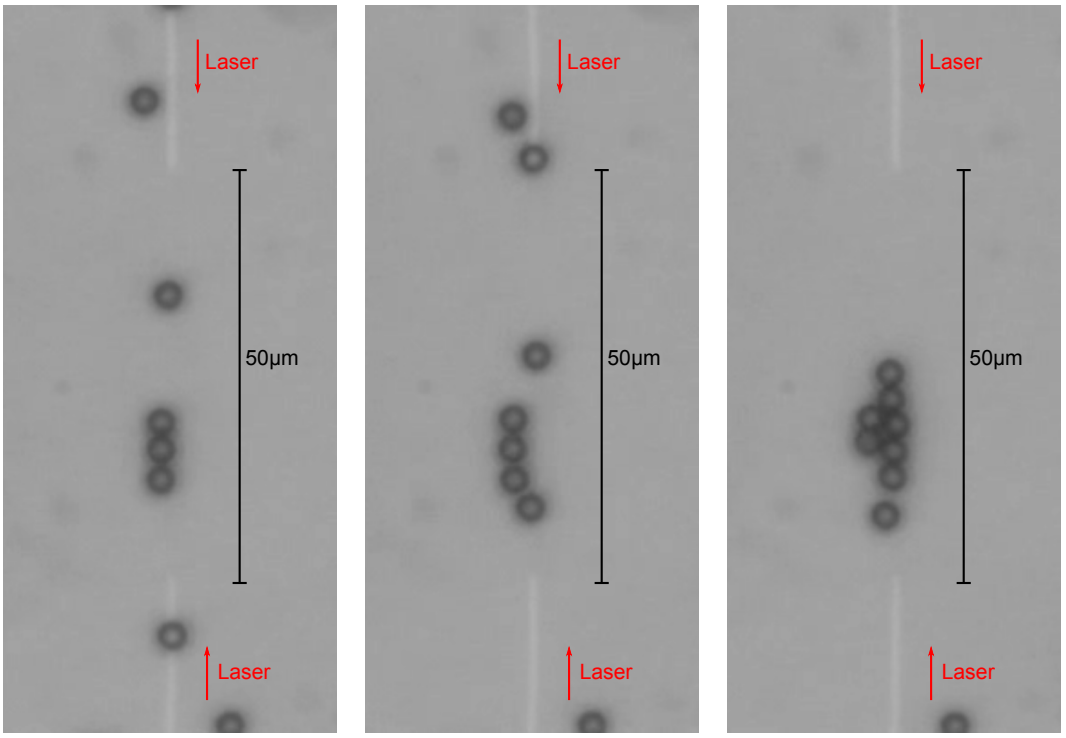

(a) 3 particles are trapped in the gap.

(b) Several other particles are approaching

(c) Many particles are trapped in the gap.

FIGURE 5.4: Trapping $3\mu m$ big particles in a $50\mu m$ wide gap on a rib waveguide. The downward gradient force makes room for more than one particle in the trap.

By altering the power balance in the arms of the waveguide loop the trapping location can be moved, thus the particles position can be controlled when they are trapped in the gap of a rib waveguide. This can be seen in **Movie 10**. Figure 5.5(a) is a frame from the movie that show 2 particles trapped in a 20 μm big gap. By changing the input stages transverse coupling we are able to shift the power balance in the two waveguide loop arms. In figure 5.5(b) the power from the top arm is bigger than the lower arm, thus the stable trapping location change its position. The particles are seeking towards the highest gradient and are thus manipulated to follow the trap as it moves in the gap. By moving the input stage in the opposite direction, the trapping location is moved accordingly as seen in figure 5.5(c).

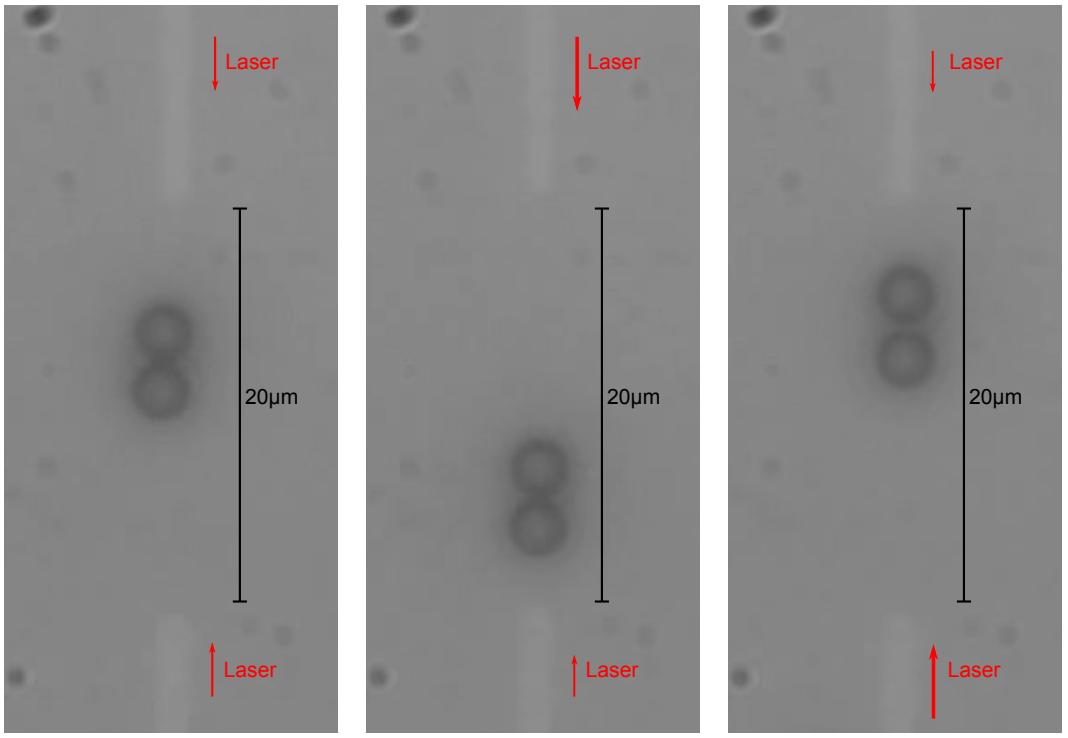

(a) Particles stably trapped in the gap

(b) By altering the power balance in the arms, the particles move towards the opposite arm

(c) More power in the lower arm, and the particles move to the other side

FIGURE 5.5: Manipulating $3\mu m$ big particles in a $20\mu m$ wide gap on a rib waveguide. The trapping location depend on the power balance in the arms of the loop.

5.2 Trapping $1\mu m$ big particles in the gap of rib waveguides

To further investigate how several particles acts in the gap of a rib waveguide loop, $1\mu m$ big particles were trapped in a $20\mu m$ wide gap. The particles position where manipulated by altering the power in the waveguide arms. This can be seen in **Movie 11**. Figure 5.6 shows three frames from the movie where we can see that the particles form a cluster as they are trapped near the center of the waveguide, and form lines when they are trapped near the waveguide ends.

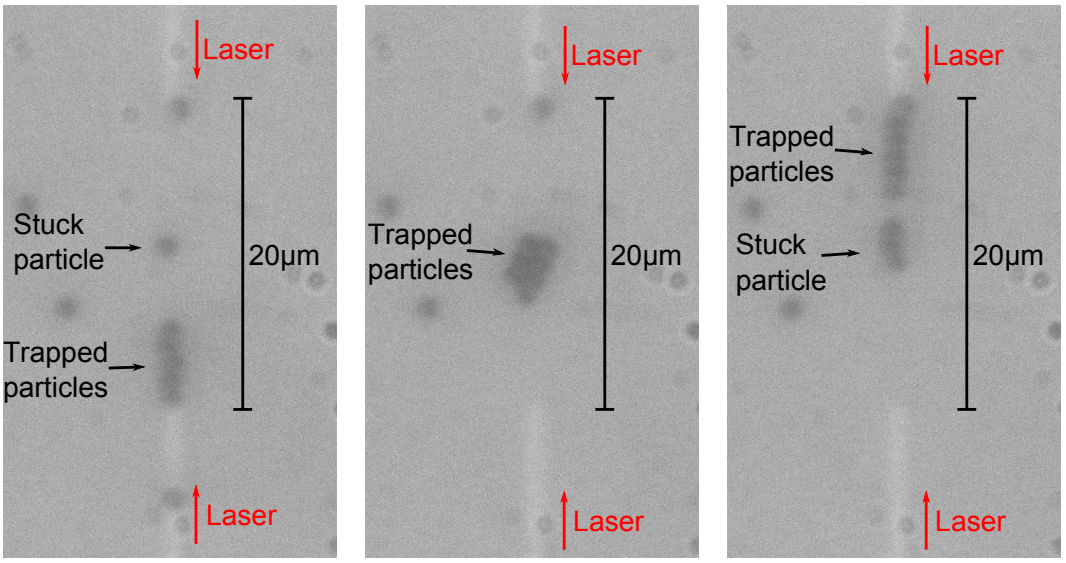

(a) Particles are trapped at the lower arm, forming a line

(b) Particles trapped near the center, forming a cluster

(c) Particles are trapped at the top arm, forming a line

FIGURE 5.6: Trapping many $1\mu m$ big particles in a $20\mu m$ wide gap on a rib waveguide. The particles form cluster near the center of the gap, and lines near the ends of the waveguides.

Chapter 6

Discussion

6.1 Tracking of fluorescent particles on strip waveguides

6.1.1 Tracking on straight waveguides

In this thesis we have seen waveguide trapping of microparticles on both strip and rib waveguides. Particles have been propelled on straight waveguides, and stably trapped in the gap of the waveguide loop. Fluorescence imaging has been used together with an algorithm to track the motion of particles trapped on strip waveguides. The method and algorithm was found to have a lower limit of detection, i.e a noise threshold. This was found by off-focus imaging of immobilized fluorescent particles, and analyzing the diffraction rings with the tracking algorithm. A measurement of the lower detection limit is the average of the straight line fit through the vertical tracking of the particles as found in section 4.2, i.e $\bar{\sigma}_{z(error)} = \underline{50.2nm}$.

Noise contributed by the imaging setup can be kept to a minimum by having all clean surfaces to work with, especially the CCD chip on the camera, but also clean filters and lenses throughout the microscope. Noise contributed by the algorithm is somewhat linked to the quality of the images used, which again is linked to the equipment and setup. Small detection errors in the algorithm will produce a big impact on the result, as an error of one pixel in the detection of the radius of the outermost diffraction ring will correspond to vertical displacements of around $200nm$. We saw that noise contributed by angles in the setup and photo-bleaching of the particles gave the same impact on the results. Slow linear drift was the result in both cases as can be seen in figures 4.3(a) and 4.5(a). The linear trend was corrected by subtracting a straight line fit from all the measurements. The most prominent noise contributed, is believed to come from non-uniformity of the laser used for exciting the fluorescence. If the illumination was perfectly uniform over

the whole field of view the particle would glow at the same intensity for the whole measurement, but as was experienced, particles wandered in and out of local maxima providing the tracking algorithm with images indicating more vertical displacement than there really was. This is best shown in figures 4.5(a) and 4.5(b) where we see the impact that a bright frame (frame 28) has on the detected vertical displacement. The problem of non-uniform illumination was due to the challenges associated with the experimental setup. The $532nm$ (excitation laser) was fibre-coupled and the laser module was retro-fit on to a standard observation microscope by inserting appropriate dichroic mirrors. The setup was optimized several times, but perfect uniform excitation of the $532nm$ laser was not achieved. A microscope specially made for fluorescence microscopy may provide a more uniform excitation field.

500nm particles were found unsuitable to use with the algorithm as they gave poor fluorescent signals, that together with high propulsion speeds produced images of low quality. $1\mu m$ big particles produced a stronger fluorescent signal and several movies were found good enough to analyze. The particles vertical movement on straight waveguides was tracked resulting in an average standard deviation of $\bar{\sigma}_z = \underline{62.6nm \pm 6.35nm}$. The maximum displacement was measured to be $\delta z_{max} = \underline{292nm \pm 38.7nm}$ after linear trends had been removed. These results are in the same range as the noise. We saw a slight improvement in the standard deviation after removing frames corrupted by noise, but the lower detection threshold of $\bar{\sigma}_{z(error)} = \underline{50.2nm}$ was not surpassed. The conclusion from this is that the particle stays within the evanescent field as it propels forwards. The particle may be wobbling as it propels along the waveguide, but the motion is within the range of the evanescent field.

For particles with a diameter of $2\mu m$ the achieved average standard deviation was $\bar{\sigma}_z = \underline{54.6nm \pm 2.83nm}$. The movies acquired of $2\mu m$ big particles were inspected as the best movies of the experiments regarding the noise. The result from the vertical tracking is stable as can be seen from the low error of $\bar{\sigma}_z$. The particles are again seen to stay within the evanescent field as they propel along the waveguide.

The results of vertical tracking of the $3.87\mu m$ big particles are seen in table 4.10 where we see the average standard deviation of $\bar{\sigma}_z = \underline{85.2 \pm 9.38nm}$. This result show a bit more vertical movement than the preceding results, and may be caused by vertical movement of the particles. The particles are almost twice as large as the $2\mu m$ big particles and the evanescent field only reaches about $600nm - 700nm$ above the waveguide, but is most prominent at $150nm - 200nm$. The particles are thus only affected by the evanescent field in a small region.

6.1.2 Tracking in the gap of a strip waveguide

In this thesis we successfully demonstrated optical levitation of microparticles trapped in a $10\mu m$ big gap on a strip waveguide loop. Simulations predicted the levitation and it was experimentally verified during the work of this thesis. Particles of different sizes ($1\mu m, 2\mu m$ and $3.87\mu m$) were trapped and levitated by the opposing fields in the gap, and the tracking algorithm was used to successfully detect the vertical displacement of the particles.

When tracking $1\mu m$ big particles in a $10\mu m$ wide gap on a strip waveguide it was experienced that the strength of the trap was weak. Most of the particles moved away from the area above the gap as soon as they had been levitated. Imperfections in the waveguide ends is believed to cause the particles to be pushed away after levitation. This can be a result of the waveguide ends not being perfectly aligned (due to fabrication errors) making the opposing fields interfere at an horizontal angle from the waveguide ends. This again causing the particles to drift off-center and the trap to loose its grip. It was still possible to measure the average vertical displacement of the particles as $\bar{z}_w = \underline{5.63\mu m \pm 91nm}$ as seen in table 4.11. We can conclude that asymmetry of the waveguide ends is causing the trap to become weak.

$2\mu m$ big particles were trapped at an weighted average of $\bar{z}_w = \underline{663nm \pm 76.9nm}$ as seen in table 4.12. The simulation in figure 3.7(a) predicts the levitation to be either around $1.2\mu m$ or $3.2\mu m$ above the chip. Since the simulations are based on 100% symmetry of the waveguide ends, it is fair to believe that the actual experimental result would differ from the simulated result. A relative large variation in the levitation distance ($522nm - 2.35\mu m$) suggest that experimental factors play an important role in the result. These factors include power, coupling efficiency, waveguide imperfections and more. The choice of waveguide chip is probably the most prominent experimental factor, as the measurements were done using several waveguide chips. The horizontal (x-direction) distance from the waveguide ends that the particles were trapped was $\bar{x}_w = \underline{6.54\mu m \pm 90.7nm}$. The simulated horizontal (x-direction) force in figure 3.6(c) show positions offering a restoring force several places along the gap, which is comparable to the experimental result. To describe the horizontal (x-direction) movement of particles trapped in the gap, we can use the average of the individual standard deviations of the last column of table 4.12. This gives an average standard deviation of $250nm$, which describes the particles longitudinal wobble around the mean trapping distance ($\bar{x}_w$) from the waveguide end. This quantity is called the trap stiffness and is by this result confirmed to be within the range of a single interference fringe, i.e $\lambda/2n$ [8] where λ is the laser wavelength and n is the refractive index of water.

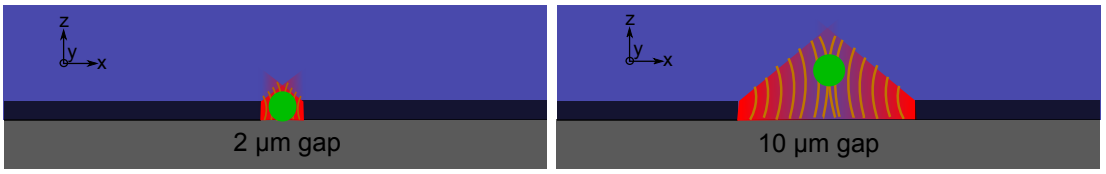

(a) Particle trapped in $2\mu m$ big gap

(b) Particle trapped in $10\mu m$ big gap

FIGURE 6.1: Side view of particle trapped in the gap of a strip waveguide. (a) In a $2\mu m$ big gap the fields have not diverged far, thus no levitation is seen. (b) In a $10\mu m$ big gap the fields have diverged further creating trapping location above the waveguide chip.

If we compare **movie 5** and **movie 6**, we notice that the the $2\mu m$ big particle (in **movie 6**) is trapped without any noticeable angle in reference to the waveguide ends. This is believed to be caused by the waveguide ends being symmetric. The particle in **movie 5** ($1\mu m$ big particle) is loosely trapped at an angle showing the asymmetry of the waveguide ends. To trap particles on strip waveguides with a gap separation of $10\mu m$ it is thus important to reduce fabrication errors in the alignment of the waveguide ends.

The result of tracking a $3.87\mu m$ big particle ended up in a small vertical displacement of $z = \underline{317nm \pm 35nm}$. The result demands more experiments to be verified. As a future experiment a larger particle should be used to see if the vertical displacement is present or not as it interacts with the gap.

The results from all these experiments have shown that the as the gap separation of a strip waveguide loop increases, the fields in the gap are given room to diverge causing particles trapped in the gap to be levitated. Earlier experiments [8] showed that particles are stably trapped for small gap separation ($2\mu m$). These particles are believed not to be levitated as the counter diverging fields interfere close to the waveguide chip. Figure 6.1 illustrates this point where we see a particle trapped in a $2\mu m$ big gap, and in a $10\mu m$ big gap . If the gap separation is increased even further ($20\mu m - 50\mu m$) the fields will diverge more causing the trap to become weak, and eventually to weak to hold the particles.

6.2 Waveguide trapping on rib waveguides

The strip waveguide loop was found to offer a weak trap when the gap separation increased ($> 10\mu m$). This drawback of the strip waveguide was overcome by the use of rib waveguide loops. Particles are successfully trapped in the gap of the rib waveguides. The trap was experienced to be more stable on rib waveguides than on strip waveguides. We saw that the strip waveguides only offered trapping for one particle in the gap, while the rib waveguides were seen to offer trapping for several particles at the same time.

By altering the power in the rib waveguide loop arms, the stable trapping position could be manipulated. The particles could thus be moved back and fourth within the gap. This might be useful for imaging/analyzing purposes. If an imaging module is fixed to analyze particles at a given point along the gap, the particles can be trapped in the gap and moved to the correct location to be analyzed.

Groups of particles trapped in the gap on rib waveguide loops were experienced to form parallel lines, or clusters when the trap was near the middle of the gap. This is believed to be caused by the diverging fields out of the waveguide ends. For a rib waveguide, the field propagating in the waveguide loop will split as it enters the gap. One part will be coupled on to the guiding layer in the gap creating an evanescent field, while one part will rapidly diverge out of the waveguide ends. The guided field in the gap will diverge slowly, and thus the evanescent field also. This is believed to cause the clustering near the center of the gap, and the formation of lines near the waveguide ends. Figure 6.2 illustrates this point where we see the guided field in the gap diverging, creating a wider trap in the center of the gap, and a narrow trap near the waveguide ends.

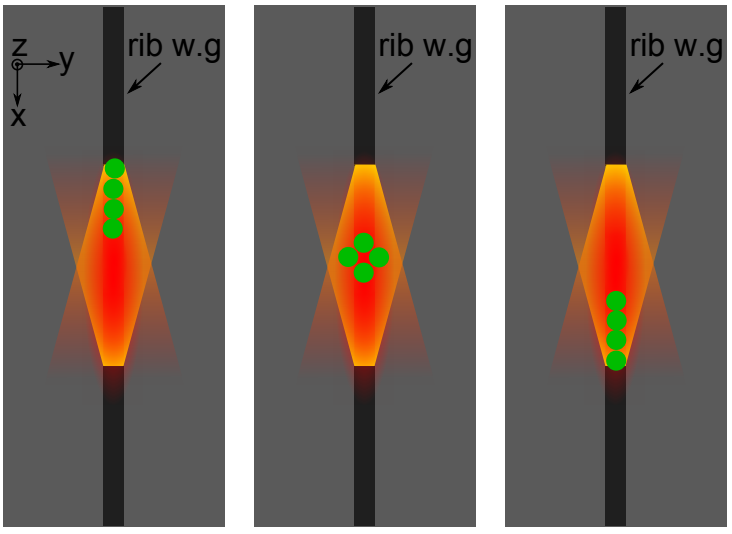

(a) Particles trapped near the end of waveguide in the gap of a rib waveguide

(b) Particles form cluster near the center due to diverging evanescent field.

(c) Particles trapped near the end of waveguide in the gap of a rib waveguide

FIGURE 6.2: Top view of particles trapped in the gap on a rib waveguide. The fields are counter-propagating in the guiding layer in the gap, and are diverging slowly. This might cause the particles to form lines when trapped near the waveguide ends as seen in (a) and (c). (b) Near the center the divergence has reach further making room for more particles width-wise.

6.3 Further work

Tracking of particles with a diameter of 500nm was difficult. The fluorescent signal produced by the particular 500nm fluorescent particles from Phosforex was weak, and together with fast propulsion the resulting images were not good enough to use with the tracking algorithm. Since the exposure time must be increased as the intensity of the fluorescent particles decrease, the best way of improving the images is to get a stronger fluorescent signal by using more power to excite fluorescence. This may cause rapid photo-bleaching of the particles so a balance must be found. It is easy to understand that smaller particles will produce a weaker signal, so it might be that 500nm big particles are to small to produce the required fluorescent signal. Trying particles from a different manufacturer can be a last resort.

A method for improving the detection of vertical displacement of microparticles propelling on straight waveguides, may be to use a waveguide excitation technique. In waveguide excitation the exciting laser is used as the trapping laser coupled on to the waveguide. This implies that both trapping and excitation of fluorescence will be achieved through the waveguide. This method might improve the noise contributed by a non-uniform excitation field experienced when exciting fluorescence from above. A problem that has to be solved using this technique is the high propagation loss experienced when using a smaller wavelength in the waveguide, i.e $532nm$ instead of $1070nm$. The propagation loss will increase rapidly as the wavelength of the laser decreases.

To improve the current setup for detecting small vertical displacements may be to reduce the mechanical noise contributed by vibrations and mechanical drift in the setup. The use of stabilizing stags, counter weights and other stabilizing equipment might improve this type of noise.

The work done in this thesis is intended to be published in two separate papers during 2014. The titles of the papers are not finalized:

- Ø.I. Helle, O.G. Hellesø and B.S. Ahluwalia. Optical levitation of microparticles on a waveguide loop. Manuscript in preparation for *Lab-On-A-Chip*, 2014.
- O.G. Hellesø, Ø.I. Helle and B.S. Ahluwalia. Study of rib waveguides for trapping and transport of microparticles. Manuscript in preparation for *Opt. Express*, 2014.

Appendix A

Contents of CD

The CD contains movies associated with the experiments done in this thesis.

- **Movie 1:** Particles with a diameter of $5\mu m$ and $3\mu m$ propelling on a straight waveguide. The smallest particles are meandering as they propel on the waveguides indicating higher order modes in the waveguide.
- **Movie 2:** $3\mu m$ big particles propelling on loop waveguide with a radius of $100\mu m$. Particles are being trapped by the waveguide, and delivered to the gap with by the loop arms. Movie from [8].
- **Movie 3:** A $3\mu m$ big particle trapped in a gap of gap-separation $10\mu m$ on a strip waveguide. Movie from [8]
- **Movie 4:** Fluorescent particle propelling on straight waveguide. The radius of the outermost diffraction ring is being tracked throughout the movie, and used to detect the vertical displacement of the particle as it propels along the waveguide.
- **Movie 5:** $1\mu m$ big fluorescent particle trapped in the gap of a strip waveguide loop. The diffraction ring becomes smaller as it enters the gap, indicating levitation. The particle is trapped off-center due to misalignment of the waveguide ends (due to fabrication error). Another particle enters the gap and knocks away the trapped particle.
- **Movie 6:** $2\mu m$ big fluorescent particle trapped in the gap of a strip waveguide loop. The radius of the outermost diffraction ring is tracked throughout the movie. The center of the particle is also tracked.
- **Movie 7:** Bright field movie of particle being knocked out of the gap on a strip waveguide loop.

- **Movie 8:** Bright field movie of 2 $3\mu m$ big particles being trapped on in the gap of a rib waveguide loop. The rib waveguide offers a downward attractive force in the gap, enabling more than one particle to be trapped at the same time.
- **Movie 9:** Bright field movie of many $3\mu m$ big particles being trapped on in the gap of a rib waveguide loop.
- **Movie 10:** Manipulating the position of particles trapped in the gap of a rib waveguide loop. By altering the power balance in the arms of the waveguide loop, the stable trapping locations is moved along the gap.
- **Movie 11:** Bright field movie of many $1\mu m$ big particles being trapped on in the gap of a rib waveguide loop and manipulated by changing the power-balance in the arms. The particles seem to form lines near the waveguide ends, and a cluster near the center.

Bibliography

[1] A. Ashkin. Acceleration and trapping of particles by radiation pressure. *Phys. Rev. Lett.*, 24:156–159, Jan 1970. doi: 10.1103/PhysRevLett.24.156. URL http://link.aps.org/doi/10.1103/PhysRevLett.24.156.

[2] B.E.A. Saleh and M.C. Teich. *Fundamentals of Photonics*. Wiley Series in Pure and Applied Optics. Wiley, 2007. ISBN 9780471358329. URL http://books.google.no/books?id=Ve8eAQAAIAAJ.

[3] Satoshi Kawata and Tadao Sugiura. Movement of micrometer-sized particles in the evanescent field of a laser beam. *Opt. Lett.*, 17(11):772–774, Jun 1992. doi: 10.1364/OL.17.000772. URL http://ol.osa.org/abstract.cfm?URI=ol-17-11-772.

[4] S. Kawata and T. Tani. Optically driven mie particles in an evanescent field along a channeled waveguide. *Opt. Lett.*, 21(21):1768–1770, Nov 1996. doi: 10.1364/OL.21.001768. URL http://ol.osa.org/abstract.cfm?URI=ol-21-21-1768.

[5] K. Grujic, O.G. Hellesø, J.S. Wilkinson, and J.P. Hole. Optical propulsion of microspheres along a channel waveguide produced by cs+ ion-exchange in glass. *Optics Communications*, 239(4–6):227 – 235, 2004. ISSN 0030-4018. doi: http://dx.doi.org/10.1016/j.optcom.2004.05.037. URL http://www.sciencedirect.com/science/article/pii/S0030401804005346.

[6] Katarina Grujic and Olav Gaute Hellesø. Dielectric microsphere manipulation and chain assembly by counter-propagating waves in a channel waveguide. *Opt. Express*, 15(10):6470–6477, May 2007. doi: 10.1364/OE.15.006470. URL http://www.opticsexpress.org/abstract.cfm?URI=oe-15-10-6470.

[7] Balpreet S. Ahluwalia and Olav G. Hellesø. Optical waveguide loop for planar trapping of blood cells and microspheres, 2013. URL http://dx.doi.org/10.1117/12.2023945.

[8] Olav Gaute Helleso, Pal Lovhaugen, Ananth Z. Subramanian, James S. Wilkinson, and Balpreet Singh Ahluwalia. Surface transport and stable trapping of particles

and cells by an optical waveguide loop. *Lab Chip*, 12:3436–3440, 2012. doi: 10.1039/C2LC40375G. URL http://dx.doi.org/10.1039/C2LC40375G.

[9] Petter Brox. Particle tracking in 3d. Master's thesis, University of Tromsoe, 2013.

[10] wikipedia webpage (accessed 24.10.2013. URL http://en.wikipedia.org/wiki/File:RefractionReflextion.svg.

[11] D.L. Lee. *Electromagnetic principles of integrated optics*. Wiley, 1986. ISBN 9780471879787. URL http://books.google.no/books?id=GOJRAAAAMAAJ.

[12] F. de Fornel. *Evanescent Waves: From Newtonian Optics to Atomic Optics*. Physics and astronomy online library. Springer, 2001. ISBN 9783540658450. URL http://books.google.no/books?id=-Eklx2aMY5AC.

[13] J.A. Stratton, IEEE Antennas, and Propagation Society. *Electromagnetic Theory*. An IEEE Press classic reissue. Wiley, 2007. ISBN 9780470131534. URL http://books.google.no/books?id=zFeWdS2luE4C.

[14] SPIE webpage on Optics documentation (accessed 12.12.2013). URL http://spie.org/Documents/Publications/00%20STEP%20Module%2008.pdf.

[15] Nature webpage (accessed 27.10.2013). URL http://www.nature.com/nature/supplements/insights/labonachip/.

[16] SPIE webpage (accessed 1.11.2013). URL http://spie.org/x32276.xml.

[17] Paal Loevhaugen. *Optical Forces, Waveguides and Micro Raman Spectroscopy*. PhD thesis, University of Tromsoe, 2012.

[18] R.G. Hunsperger. *Integrated Optics: Theory and Technology*. Advanced texts in physics. Springer, 2009. ISBN 9780387897752. URL http://books.google.no/books?id=ewOb3SbMXnUC.

[19] Jason Beech and Henrik Persson. URL http://nanobio.ftf.lth.se/~biokurs/labs/Lab4_Tweezers2014.pdf.

[20] Balpreet Singh Ahluwalia, Peter McCourt, Thomas Huser, and Olav Gaute Hellesø. Optical trapping and propulsion of red blood cells on waveguide surfaces. *Opt. Express*, 18(20):21053–21061, Sep 2010. doi: 10.1364/OE.18.021053. URL http://www.opticsexpress.org/abstract.cfm?URI=oe-18-20-21053.

[21] Katarina Grujic. *Manipulation of Microspheres with Integrated Optics*. PhD thesis, University of Tromsoe, 2007.

[22] Molecular Expressions website(accessed 19.11.2013). URL http://micro.magnet.fsu.edu/primer/anatomy/numaperture.html.

[23] Newport webpage (accessed 13.12.2013), . URL http://www.newport.com/Microscope-Objective-Lenses/141071/1033/info.aspx.

[24] zeiss-campus webpage(accessed 19.11.2013). URL http://zeiss-campus.magnet.fsu.edu/tutorials/basics/substagecondensernumericaperture/index.html.

[25] Olympys webpage (accessed 13.12.2013), . URL http://www.olympusmicro.com/primer/techniques/darkfield.html.

[26] answers.com webpage (accessed 12.11.2013). URL http://www.answers.com/topic/stokes-shift.

[27] Wikipedia webpage about fluorescence microscopy (accessed 09.12.2013). URL http://en.wikipedia.org/wiki/Fluorescence_microscope.

[28] Leica webpage (accessed 13.12.2013), . URL http://www.leica-microsystems.com/science-lab/total-internal-reflection-fluorescence-tirf-microscopy/.

[29] H.M. Grandin, B. Städler, M. Textor, and J. Vörös. Waveguide excitation fluorescence microscopy: A new tool for sensing and imaging the biointerface. *Biosensors and Bioelectronics*, 21(8):1476 – 1482, 2006. ISSN 0956-5663. doi: http://dx.doi.org/10.1016/j.bios.2005.06.011. URL http://www.sciencedirect.com/science/article/pii/S0956566305002046.

[30] Bjorn Agnarsson, Saevar Ingthorsson, Thorarinn Gudjonsson, and Kristjan Leosson. Evanescent-wave fluorescence microscopy using symmetric planar waveguides. *Opt. Express*, 17(7):5075–5082, Mar 2009. doi: 10.1364/OE.17.005075. URL http://www.opticsexpress.org/abstract.cfm?URI=oe-17-7-5075.

[31] The Leake group of Single-Molecule Cellular Biophysics webpage (accessed 13.11.2013). URL http://www.physics.ox.ac.uk/Users/leake/research/tirf.html.

[32] Goldastro webpage (accessed 05.05.2014). URL http://www.goldastro.com/goldfocus/resolving_power.php.

[33] wikipedia (accessed 05.05.2014). URL http://en.wikipedia.org/wiki/Lens_(optics).

[34] G. Brambilla, G. Senthil Murugan, J. S. Wilkinson, and D. J. Richardson. Optical manipulation of microspheres along a subwavelength optical wire. *Opt. Lett.*, 32

(20):3041–3043, Oct 2007. doi: 10.1364/OL.32.003041. URL http://ol.osa.org/abstract.cfm?URI=ol-32-20-3041.

[35] Michael Speidel, Alexandr Jonáš, and Ernst-Ludwig Florin. Three-dimensional tracking of fluorescent nanoparticles with subnanometer precision by use of off-focus imaging. *Opt. Lett.*, 28(2):69–71, Jan 2003. doi: 10.1364/OL.28.000069. URL http://ol.osa.org/abstract.cfm?URI=ol-28-2-69.

[36] J.R. Taylor. *An Introduction to Error Analysis: The Study of Uncertainties in Physical Measurements*. A series of books in physics. University Science Books, 1997. ISBN 9780935702750. URL http://books.google.no/books?id=giFQcZub80oC.